JOURNAL OF COMPUTATIONAL PHYSICS 50, 270–306 (1983)

A Numerical Method Based on the Fourier-Fourier Transform Approach for Modeling 1-D Electron Plasma Evolution

ALEXANDER J. KLIMAS

NASA/Goddard Space Flight Center, Laboratory for Extraterrestrial Physics, Greenbelt, Maryland 20771

Received December 23, 1981; revised July 20, 1982

A numerical method for studying one-dimensional electron plasma evolution under typical interplanetary conditions is presented. The method uses the Fourier–Fourier transform approach to a plasma model which is a generalization of the electrostatic Vlasov–Poisson system of equations. Conservation laws which are modified to include the plasma model generalization and also the boundary effects of nonperiodic solutions are given. A new conservation law for entropy in the transformed space is introduced. These conservation laws are used to check the accuracy of the numerical solutions. A discretization error analysis is given. Two numerical instabilities and the methods used for their suppression are discussed. Several solution examples are presented. Two of these are comparisons with earlier independent results; the comparison is favorable. A third example is also discussed which uses an interplanetary observation of a bump-on-tail unstable velocity distribution as initial data. It is shown that in interplanetary plasma conditions the bump-on-tail instability leads to significant excitation of plasma oscillations at the Bohm–Gross frequency and its second harmonic. An explanation of the second harmonic excitation in terms of wave–wave coupling during the growth phase of the instability is given.

I. INTRODUCTION

The ISEE spacecraft [1] have stimulated a detailed examination of the complicated plasma phenomena occurring in the region of space in front of the Earth's bow shock called the foreshock [2]. Of particular interest here are the energetic electrons which propagate upstream in the solar wind flow, from the bow shock into the foreshock region, along interplanetary magnetic field [3]. These electrons lead to significant heating of the plasma in the foreshock region as well as to the generation of intense electrostatic turbulence. From direct electron and electric field measurements it has been found that the electrostatic plasma behavior is largely one dimensional with the magnetic field providing the direction in space for this dimension.

In this paper a numerical method for modeling the one-dimensional electron plasma behavior in the foreshock region is presented. This method is based on a plasma model which is a generalization of the electrostatic Vlasov–Poisson system of equations. The Vlasov–Poisson system does not determine the evolution of the space

0021-9991/83 $3.00

average of the electric field which may play an important role in the foreshock. The equation due to Maxwell which contains his displacement current is added to the Vlasov–Poisson system in order to complete the plasma description. A detailed discussion of this issue is given by Klimas and Cooper [4].

The plasma equations are Fourier–Fourier transformed both in the position and the velocity variables following the technique introduced by Knorr [5]. The result is further reduced using a transformation of dependent variables introduced by Klimas [6] to obtain a semi-linear system of hyperbolic partial differential equations in the normal form [7]. Except for an additional term due to the inclusion of nonperiodic solutions, this system of equations is identical to that obtained by Knorr. However, the dependent variables are not the characteristic functions of the electron distribution function as they are in the Knorr equations; they are related to the characteristic functions through the transformation given by Klimas. The conservation laws for the plasma given by Knorr must be modified for the generalized plasma model considered here. For solutions periodic in the position variable the total number of particles in the region of periodicity is still conserved but the total particle momentum is not. The total energy of the plasma is modified due to the presence of the space-averaged electric field. The necessary modifications of these conservation laws are presented here. Since the method presented here is not limited to periodic solutions, further modifications of the conservation laws for nonperiodic solutions are also given.

An additional conservation law for entropy which has not been considered before in attempts to integrate the Knorr equations is introduced here. This is an important consideration for checking the accuracy of these numerical solutions. The conservation laws mentioned in the previous paragraph follow from a moment expansion of the electron distribution function which translates into a power series expansion about the origin of the Fourier variable complimentary to velocity in the Fourier–Fourier transformed space. Those conservation laws can be used to test the accuracy of the solution only at the origin of the Fourier variable; they are local conservation laws. A calculation of the entropy in the transformed space requires integration over the Fourier variable and summation over the modes. For entropy conservation the solution must remain accurate over all of the transformed space for all of the modes. The local conservation laws and the entropy conservation law together provide a much more rigorous test for the accuracy of the solution than either alone. The numerical calculations which are presented in this paper have been monitored to ensure the satisfaction of both types of conservation laws.

The Knorr equations have been discussed in several papers and various methods have been used to integrate them numerically [8–12]. The method of integration used here is closely related to that used by Denavit [9] and by Denavit and Kruer [10] with several modifications which were judged necessary to make the solutions useful in space physics applications. A higher order discretization scheme is used. An analysis is given which shows that the discretization error is formally fifth order in the grid spacing but nonuniformly so over the grid. A method for handling the nonuniformity is discussed. The difference equations are implicit; they require a

matrix inversion to march forward on the grid. The matrix inversion is carried out iteratively on a grid with fixed spacing. The number of iterations done at each grid is varied in such a way as to allow a larger grid spacing over all the grid. The boundary of the grid is varied so that the solution is calculated only where it is effectively nonzero. Conversely, regions of the grid where the solutions is nonzero are not discarded. Two numerical instabilities have been discovered. The sources of these instabilities are discussed and methods for their removal are presented. The result is a numerical code for integrating the Knorr equations which is almost certainly slower than that used, for example, by Denavit and Kruer but which is stable and accurate over long integration times. In application this code is typically being used to integrate to approximately one hundred plasma periods ($\omega_p t \gtrsim 600$) with no significant degradation in the conservation laws and no apparent unstable behavior. An example of such an application is given here.

Cheng and Knorr [13] have developed an entirely different "splitting" scheme for integrating a subset of the equations considered by Klimas without the Fourier–Fourier transformation. Gagné and Shoucri [14] have developed this splitting method further and recently Shoucri [15] has presented a numerical study of a bump-on-tail instability using the same method. It can be shown that in some circumstances [16] solutions of the subset of equations considered by these authors are also solutions of the set considered by Klimas. The examples presented by Cheng and Knorr fall into this class. The integration method presented here has been used to recompute the examples presented by Cheng and Knorr. A comparison of the results is given in Section VI. The comparison is favorable; only very small differences emerge. Thus, the results of Cheng and Knorr have been confirmed and the viability of the alternative integration scheme which is presented here has been established.

An additional example is presented which, for initial data, uses an electron velocity distribution observed in the foreshock region aboard the ISEE-1 spacecraft by the GSFC Electron Spectrometer Experiment. This data shows the first bump-on-tail reduced velocity distribution observed in the foreshock region; its existence has been postulated for years [17, 18]. Thus, this example shows the evolution of a bump-on-tail plasma instability in the interplanetary plasma state. The evolution is surprisingly different from anything that has been found before for the bump-on-tail instability in one dimension. The initial evolution follows the predictions of linear plasma theory quite well. However, long before saturation of the instability, at a time when the linear theory is expected to apply, a reversal of the predicted exponential decay of one of the field modes occurs. Following the reversal this mode grows exponentially in time and saturates at about the same time as the overall instability *with its oscillation frequency twice the fundamental Bohm–Gross frequency.* Second harmonic plasma oscillations have often been observed in interplanetary plasma where the bump-on-tail instability is thought to be playing a role but direct electrostatic excitation of the second harmonic has not been thought possible [18–20]. The numerical solution presented here shows that second harmonic excitation is indeed possible and a simple explanation for the excitation, which is also given here, shows that it is quite likely.

II. Discretized Equations

The plasma model under consideration here has been discussed by Klimas [6]. He has shown that the problem of finding the time evolution of the 1-D electron plasma can be reduced to finding solutions of his Eq. (13) which is reproduced here using slightly modified notation.

$$K_m(v,\tau) = K_m(v - m\tau, 0) + \int_0^\tau d\lambda \sigma_m(v - m(\tau - \lambda), \lambda)$$

$$+ \int_0^\tau d\lambda [v - m(\tau - \lambda)] A_{m,n}(\lambda) K_n(v - m(\tau - \lambda), \lambda) \tag{1}$$

in which

$$\begin{aligned} A_{m,n}(\tau) &= \frac{K_{m-n}(0,\tau)}{m-n}, \qquad && (m \neq n, |m-n| \leqslant M), \\ &= 0, && (\text{otherwise}), \end{aligned} \tag{2}$$

and a summation on the index n, from $n = -M$ to $n = M$, is implied. Equation (1) governs the evolution of the $2M + 1$ ($-M \leqslant m \leqslant M$) Fourier–Fourier modes, $K_m(v, t)$, for $-\infty \leqslant v \leqslant \infty$ and $\tau \geqslant 0$.

The plasma model is subject to initial and boundary value data. The $K_m(v, 0)$ in Eq. (1) can be computed from the initial plasma data and the $\sigma_m(v, \tau)$ follow from the boundary value data. Thus, Eq. (1) is to be studied as an initial value problem with the $K_m(v, 0)$ and $\sigma_m(v, \tau)$ given. For solutions with periodic boundary data $\sigma_m(v, \tau) = 0$.

When $\sigma_m = 0$, Eq. (1) is essentially identical to an equation given by Knorr [5, Eq. (40)] for the electron distribution characteristic functions in the electrostatic approximation under the assumption that the space average of the electric field is zero for all time. It is a rather remarkable fact that the plasma model under consideration here can be reduced to the system of equations derived by Knorr even though the space average of the electric field is here determined by an additional equaton of Maxwell and is not set arbitrarily to zero. The only difference which remains is that the K's is Eq. (1) are not the characteristic functions and, therefore, a physical interpretation of the solution of Eq. (1) must be appropriately modified. It would be incorrect to assume that in the foreshock region, just in front of the earth's bow shock, the space average of the electric field is zero. This assumption would be particularly inconsistent when nonperiodic solutions are considered. Thus, the application intended here makes the generalized plasma model necessary.

The initial plasma data will be assumed a "good function" [21] of velocity. Then, each of the $K_m(v, 0)$ are good functions of v; i.e., each of the $K_m(v, 0)$ is everywhere differentiable any number of times and it and all its derivatives are $O(|v|^{-N})$ as $|v| \to \infty$ for all N. In this case it is always possible, for numerical purposes, to treat

the $K_m(v, 0)$ as functions of v with compact support. In the following, truncated approximations to the $K_m(v, 0)$ will be used which are zero for $|v| > A$, where A is chosen large enough to reduce the error which is made in this truncation to an acceptable level. Then, the domain of influence on the (v, τ)-plane of the initial data is as pictured in Fig. 1. Outside the domain of influence, $K_m(v, \tau) = 0$ for all $\tau \geqslant 0$. The expansion of the domain of influence in v, with increasing τ, is the analogue in this space of the possibility of velocity space filamentation [22]. As larger values of v are reached, finer structures in the velocity distribution become possible. This numerical calculation is carried out on the domain of influence of the initial data with the following possible exception: It has been found that occasionally the $K_m(v, \tau)$ do not expand in v with increasing τ at the rate allowed. To take advantage of this possibility the $K_m(v, \tau)$ are periodically checked to see if a new domain of influence can be defined and truncated approximations to the $K_m(v, \tau)$ introduced, as at $\tau = 0$, with a new $A(\tau)$ chosen on the same basis of tolerable degree of error. Thus, the calculation may actually be carried out on a domain shown schematically by the dashed lines in Fig. 1. Notice that when this kind of evolution does occur, then strong velocity space filamentation is impossible.

In preparation for obtaining discrete approximations to its solutions, Eq. (1) can be used to find

$$K_m(v, \tau) = K_m(v - 2m\Delta\tau, \tau - 2\Delta\tau) + \int_{\tau-2\Delta\tau}^{\tau} d\lambda \sigma_m(v - m(\tau - \lambda), \lambda)$$

$$\int_{\tau-2\Delta\tau}^{\tau} d\lambda [v - m(\tau - \lambda)] A_{m,n}(\lambda) K_n(v - m(\tau - \lambda), \lambda), \tag{3}$$

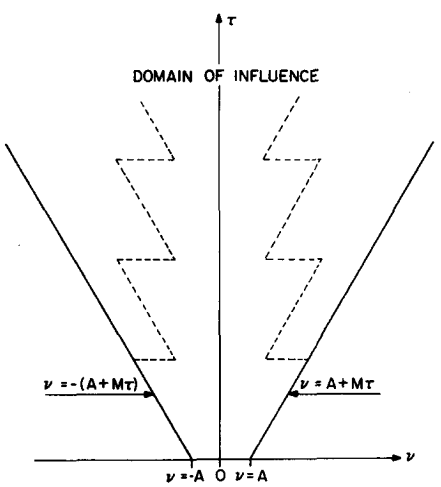

FIG. 1. The $K_m(v, \tau)$ are calculated forward in τ from $\tau = 0$ on the domain bounded by the solid lines or, when possible, on the domain bounded by the dashed lines.

where $\Delta\tau$ is the grid spacing which will be used in the following. The finite difference equation which is used here is obtained by substituting a 3-point (Simpson's rule) evaluation of the last integral in Eq. (3). On a square grid, with $v = I\Delta\tau$ and $\tau = J\Delta\tau$, the result of this substitution can be written (using vector notation) as,

$$[\mathbf{I} - \varepsilon I\mathbf{A}(J)] \cdot \mathbf{h}(I, J) = \mathbf{g}(I, J), \tag{4}$$

in which the vector component $h_m\ (I, J)$ is the discrete approximation to the mode $K_{m-M-1}(v, \tau)$, now with $1 \leqslant m \leqslant 2M + 1$. In this equation $\varepsilon = \frac{1}{3}(\Delta\tau)^2$.

$$\begin{aligned} A_{m,n}(J) &= \frac{h_{m-n+M+1}(0, J)}{m - n}, \qquad (m \neq n, |m - n| \leqslant M, 1 \leqslant m, n \leqslant 2M + 1), \\ &= 0, \qquad\qquad\qquad (\text{otherwise}), \end{aligned} \tag{5}$$

and

$$\begin{aligned} g_m(I, J) = h_m(I - 2(m - M - 1), J - 2) + S_m(I, J) \\ + \varepsilon[4(I - (m - M - 1))\, C_m(I - (m - M - 1), J - 1) \\ + (I - 2(m - M - 1))\, C_m(I - 2(m - M - 1), J - 2)], \end{aligned} \tag{6}$$

in which

$$C_m(I, J) = A_{m,n}(J)\, h_n(I, J) \tag{7}$$

and

$$S_m(I, J) = \int_{(J-2)\Delta\tau}^{J\Delta\tau} d\lambda \sigma_{m-M-1}(I\Delta\tau - (m - M - 1)(J\Delta\tau - \lambda), \lambda). \tag{8}$$

With this formulation, the problem of finding a numerical approximation to the solutions of nonlinear Eq. (1) is reduced to the essentially linear matrix inversion.

$$\mathbf{h}(I, J) = [\mathbf{I} - \varepsilon I\mathbf{A}(J)]^{-1} \cdot \mathbf{g}(I, J). \tag{9}$$

Given $\mathbf{h}(I, J - 1)$ and $\mathbf{h}(I, J - 2)$, $\mathbf{g}(I, J)$ can be calculated. From Eq. (4),

$$\mathbf{h}(0, J) = \mathbf{g}(0, J) \tag{10}$$

and, from Eq. (5), $\mathbf{A}(J)$ can be calculated. Equation (4) can be treated as a linear equation for $\mathbf{h}(I, J)$ with Eq. (9) for its solution. Thus, the numerical solution at two time steps can be used to compute a third time step. A two-point evaluation of the integral in Eq. 3 is used to get the calculation started.

III. Discretization Error and Matrix Inversion

The discretization error involved in approximating Eq. (3) by Eq. (4) is formally $O(\Delta\tau^5)$. However, because the linear power of ν appears under the integral sign in Eq. (3), this formal ordering is nonuniform in ν (or the index, I). Consider that contribution to the integral given by

$$\begin{aligned} I_m(\nu, \tau) &= \nu \int_{\tau - 2\Delta\tau}^{\tau} d\lambda A_{m,n}(\lambda)\, K_n(\nu - m(\tau - \lambda), \lambda) \\ &= \int_{-\Delta\tau}^{\Delta\tau} d\lambda Q_m(\nu, \tau, \lambda), \end{aligned} \tag{11}$$

where

$$Q_m(\nu, \tau, \lambda) = \nu A_{m,n}(\tau - \Delta\tau + \lambda)\, K_n(\nu - m(\Delta\tau - \lambda), \tau - \Delta\tau + \lambda). \tag{12}$$

With the assumption of the good initial data, and with reasonable restrictions on the $\sigma_m(\nu, \tau)$, it can be shown [23] that the $K_m(\nu, \tau)$ have the four derivatives (the effects of truncation at the edge of the domain of influence will be discussed shortly) necessary to carry out the standard error analysis as follows: Let $I_m(\nu, \tau) = S_m(\nu, \tau) + E_m(\nu, \tau)$, where $S_m(\nu, \tau)$ is the three-point approximation to Eq. (11) given by

$$S_m(\nu, \tau) = (\Delta\tau/3)[Q_m(\nu, \tau, \Delta\tau) + 4Q_m(\nu, \tau, 0) + Q_m(\nu, \tau, -\Delta\tau)]; \tag{13}$$

then [24]

$$|E_m(\nu, \tau)| \leqslant (G/90)(\Delta\tau)^5 \tag{14}$$

if

$$|Q_m^{(4)}(\nu, \tau, \lambda)| \leqslant G \qquad (-\Delta\tau \leqslant \lambda \leqslant \Delta\tau), \tag{15}$$

in which the (4) indicates the fourth derivative with respect to λ. Unfortunately,

$$\mathbf{Q}^{(4)}(\nu, \tau, \lambda) = [\nu \mathbf{A}(\tau - \Delta\tau + \lambda)]^5 \cdot \mathbf{K}(\nu - m(\Delta\tau - \lambda), \tau - \Delta\tau + \lambda).$$

Although in typical applications the elements of the matrix $\mathbf{A}$ are usually no larger than 10^{-3} to 10^{-2}, the discretization error can get arbitrarily large as $|\nu|$ increases. Given the tendency of the domain of influence to expand with increasing τ, values of ν large enough to make the discretization error unacceptable are encountered. To circumvent this problem, at each time step in the calculation the maximum eigenvalue of $\mathbf{A}$, $\lambda_{\max}$, is computed and the quantity $\nu_{\max} \Delta\nu\lambda_{\max}$, where $\nu_{\max}$ defines the expanding boundary of the domain of influence, is monitored. A constant C is defined so that is fifth power is equal to the error which is tolerated in the matrix inversion of Eq. (9). (The matrix inversion will be discussed shortly.) The grid spacing is chosen so that initially $\nu_{\max} \Delta\nu\lambda_{\max} < C$. If at some time step $\nu_{\max} \Delta\nu\lambda_{\max} \geqslant C$, the calculation

is stopped, the grid spacing is halved, data is computed to fill the new grid positions using an interpolation scheme, and the calculation is restarted. This chain of events is most likely to be encountered in calculations of plasma instabilities in which the rapidly rising electric field strengths lead to a rapid increase of λ_{max} with increasing τ. Although no filamentation has been encountered in this Fourier transformed space, the increase of v_{max}, and the possible increase of λ_{max}, with increasing τ, still often require shifts to finer grids as the calculation proceeds. This phenomenon will be discussed further in Section VI in relation to the individual examples of solutions that are presented there.

In view of the fact that $v_{max}\Delta v\lambda_{max}$ is always maintained small compared to one it becomes advantageous to use an iterative scheme for calculating the matrix inversion in Eq. (9). This iterative evaluation of the matrix inversion is the discrete analogue of the iterative approximation scheme dicussed by Klimas [6].

A sequence if iterates to $\mathbf{h}(I, J)$ is calculated with $\mathbf{h}(I, J; 0) = \mathbf{g}(I, J)$ and with the α'th iterate computed according to

$$\mathbf{h}(I, J; \alpha) = \mathbf{h}(I, J; 0) + \varepsilon I\mathbf{A}(J) \cdot \mathbf{h}(I, J; \alpha - 1). \tag{16}$$

Thus,

$$\mathbf{h}(I, J; \alpha) = \sum_{n=0}^{\alpha} [\varepsilon I\mathbf{A}(J)]^n \cdot \mathbf{g}(I, J) \tag{17}$$

and

$$\lim_{\alpha \to \infty} \mathbf{h}(I, J; \alpha) = [\mathbf{I} - \varepsilon I\mathbf{A}(J)]^{-1} \cdot \mathbf{g}(I, J). \tag{18}$$

With the introduction of an eigenbasis for the matrix $\mathbf{A}$, it is easy to see that the rate of convergence of the summation in Eq. (17) is controlled by λ_{max}. The maximum number of iterations at each grid point α_{max} is precalculated so that $[\varepsilon I\lambda_{max}]^{\alpha_{max}} < e_r$, where e_r is the error mentioned above in the discussion surrounding the choice of C. Notice that the convergence rate of this iterative scheme is nonuniform over the grid and that, therefore, α_{max} must increase with increasing I.

The overall method presented above for integrating the Knorr equations is similar to that used Denavit [9] and by Denavit and Kruer [10], but with several modifications. They used a first-order discretization and chose to iterate just once while adjusting the grid size at each time step to make the first iterate sufficiently accurate. They handled the nonuniformity in the iteration convergence rate mentioned above by choosing their step size small enough so that the first iterate is sufficiently accurate in the worst case when $v = v_{max}$ ($q = q_{max}$ in their notation). In the method presented here a higher order discretization on a fixed grid, with a variable number of iterations over the grid, is used. The interpolation associated with the variable grid is avoided, advantage is taken of the more rapid iteration convergence available over most of the grid interior, and the larger grid spacing which is consequently possible is

used. Finally, the variation of v_{max} with increasing time (index J) which is included here avoids serious truncation error in the solution when it does expand to fill the domain of influence of the initial data and, conversely, provides maximum efficiency when the solution does not expand. The solution is computed only where it is effectively nonzero and at the same time grid regions where the solution is nonzero are not arbitrarily discarded. Only in this way could the entropy conservation law, which is discussed in the following section, be satisfied.

IV. Conservation Laws

There are several conservation laws which are considered important for modeling the behavior of an electrostatic plasma. These have been presented by Knorr [5] in terms of the characteristic functions for the electrostatic electron distribution function. The conservation laws which apply to the plasma model under consideration here are generalizations of the Knorr results due both to the generalized plasma model and the inclusion of nonperiodic solutions. Nevertheless, these physical conservation laws, for particle number, momentum, and total plasma energy can be reduced to forms which are identical to those given by Knorr (for periodic solutions) but for quantities which are no longer physical. These reduced forms are given here. In addition, a reduced form for entropy conservation is also given. These reduced conservation laws are used to check the accuracy of the numerical solutions.

A. *Particle Number*

The total number of electrons in the region of configuration space under consideration is given by $K_0(0, \tau)$. For the fixed ion density model considered here $K_0(0, \tau)$ must be maintained constant to ensure the overall neutrality of the plasma. Thus, the boundary conditions which are applied must incorporate $\sigma_0(0, \tau) = 0$. The discrete approximation to $K_0(0, \tau)$ is given by $h_{M+1}(0, J)$. From Eqs. (4)–(8) with $\sigma_0(0, \tau) = 0$, it can be shown that $h_{M+1}(0, J) = h_{M+1}(0, J-2)$. Thus, total particle number is conserved by the discrete equations.

B. *Total Momentum*

In contrast to the case for the electrostatic plasma, the total particle momentum is not conserved. Instead, it satisfies [6, Eq. (11)]. In order for that equation to hold, however, the relationship,

$$\frac{\partial K_0'(0, \tau)}{\partial \tau} = \sigma_0'(0, \tau), \tag{19}$$

where the primes signify differentiation with respect to v, must hold. This is the reduced momentum conservation law; for periodic solutions ($\sigma_0 = 0$) it is identical in form to that given by Knorr [5] for the physical momentum, however, the characteristic function has been replaced by K_0. The value of $K_0'(0, \tau)$ is monitored to ensure approximate conservation of reduced momentum according to Eq. (19).

C. *Total Energy*

The conservation law for total energy in the plasma is given by [6, Eq. (26)]. That equation can be reduced to

$$dT(\tau)/d\tau = \sigma_0''(0, \tau), \tag{20}$$

where

$$T(\tau) = \sum_{n=-M}^{M}{}' \left| \frac{K_n(0, \tau)}{n} \right|^2 - K_0''(0, \tau), \tag{21}$$

in which the prime on the summation indicates that the term in the sum corresponding to $n = 0$ is not included. Equations 20 and 21 give the reduced energy conservation law. Again the conservation law is similar to that given by Knorr [5] but the conserved quantity is not the physical energy. The quantity $T(\tau)$ is monitored to ensure the approximate conservation of reduced energy.

D. *Entropy*

Because the K_m are closely related to the Fourier–Fourier transform of a real function, $K_m^*(v, \tau) = K_{-m}(-v, \tau)$, in which the star denotes complex conjugation. With the use of this symmetry, and Eqs. (1) and (2), it can be shown that the entropy,

$$H(\tau) = \int_{-\infty}^{\infty} dv \sum_{m=-M}^{M} |K_m|^2 \tag{22}$$

satisfies

$$\frac{dH}{d\tau} = \int_{-\infty}^{\infty} dv \sum_{m=-M}^{M} (K_m^* \sigma_m + K_m \sigma_m^*). \tag{23}$$

In the periodic plasma, for which $\sigma = 0$, the entropy is a constant. Otherwise, transport of entropy across the boundaries of the configuration space, as specified by the boundary conditions, leads to changes of the entropy given by Eq. (23).

Notice that these conservation laws for the entropy and the reduced momentum and energy provide a complimentary pair of tests for the accuracy of the numerical integration as it proceeds. The reduced momentum and energy provide for a local test in the vicinity of $v = 0$ and the entropy is global requiring integration over all v and summation over all modes at each time step. It has been found through experience that the presence of numerical instabilities is very quickly reflected in the failure of at least one of these conservation laws. The entropy test has proven particularly useful for detecting problems in the vicinity of the boundary of the domain of influence near $v = v_{\max}$. This issue will be explained fully in the next section where the numerical instabilities which have been encountered are discussed.

V. Numerical Instabilities

Two numerical instabilities have been encountered in the implementation of the integration scheme discussed above. The first of these is apparently caused by the truncation of the domain of influence at $v = v_{max}$; it is not inherent to the integration scheme itself. A brief description of this instability and its removal is given here. The second instability is more fundamental to this integration scheme. This instability and a method for removing it are the main subjects of this section.

A. *Instability at* v_{max}

The analysis of the discretization error which is presented in Section III shows that there is a tendency for that error to grow with increasing v. The domain on which this numerical integration is done is truncated in v in order to maintain this error at a tolerably low level. Unfortinately, the process of truncation introduces a discontinuity in the solution at $v = v_{max}$ which is beyond the scope of the discretization error analysis which assumes smooth solutions. It has been found that, for solutions where v_{max} approaches the maximum allowed before a halving of the grid spacing is required, a weak saw tooth-like wave sometimes appears in the numerical solution as a function of v near $v = v_{max}$. Apparently the truncation process excites this waveform. The wavelength of this disturbance is always very small and thus it is easy to detect superimposed on the relatively slow variations of the undisturbed solution. This clear separation of wavelengths also makes it possible to smooth the numerical solution in the vicinity of $v = v_{max}$ in order to prevent the propagation of the saw tooth instability into the interior of the domain of influence where it tends to grow rapidly.

B. *Instability at* $v = 0$

A second numerical instability has been encountered which is apparently excited only when the electric field modes are very small; it has never been detected otherwise. The excitation of this instability can be readily understood through the use of a linear approximation to Eqs. (4)–(8) which is appropriate when the field modes are small.

In the following, for convenience, the notation $K_m(I, J) = h_{m+M+1}(I, J)$ will be used for the discrete approximations to the $K_m(v, \tau)$, with the index m in the range $-M \leqslant m \leqslant M$. Only periodic solutions will be considered. As explained in Section IVa, $K_0(0, J) = 1$. When I is near zero, $K_0(I, J)$ is generally not very small compared to one. If the electric field modes are very small compared to one, however, then the $K_m(I, J)$ $(m \neq 0)$ are generally comparably small for all I. The linear equations mentioned above are obtained by dropping all terms in Eqs. (4)–(8) that are higher order than linear in the $K_m(I, J)$ for $m \neq 0$. The linear equations are,

$$\begin{aligned} K_m(I, J) = {} & K_m(I - 2m, J - 2) + (\varepsilon/m)[IK_m(0, J)\, K_0(I, J) \\ & + 4(I - m)\, K_m(0, J - 1)\, K_0(I - m, J - 1) \\ & + (I - 2m)\, K_m(0, J - 2)\, K_0(I - 2m, J - 2)] \end{aligned} \tag{24}$$

for $m \neq 0$, and

$$K_0(I, J) = K_0(I, J-2). \tag{25}$$

For simplicity consider a limited domain in I near $I = 0$ and in this domain let $K_0(I, J) = 1$. Then, with the introduction of $D_m(I, J) \equiv K_m(I, J) - K_m(I - 2m, J)$, and by considering Eq. (24) at $I = 0$ and $I \neq 0$, the following two equations can be constructed:

$$\begin{aligned} D_m(I, J) = {} & D_m(I - 2m, J - 2) \\ & + 2\varepsilon[K_m(0, J) + 4K_m(0, J-1) + K_m(0, J-2)] \end{aligned} \tag{26}$$

and

$$\begin{aligned} K_m(0, J) = {} & K_m(0, J-2) - D_m(0, J-2) \\ & - 2\varepsilon[2K_m(0, J-1) + K_m(0, J-2)]. \end{aligned} \tag{27}$$

Now, suppose $K_m(0, J-2) > 0$ and $K_m(0, J-1) < 0$ but both are comparable in magnitude, and also suppose $D_m(0, J-2) < 0$ and small (i.e., gradients are finite and grid spacing is small). Then, from Eq. (27), $K_m(0, J) > K_m(0, J-2)$ by a small amount and, from Eq. (26), $D_m(I, J) < D_m(I - 2m, J - 2)$ by a small amount. If, on the other hand, $K_m(0, J-2) < 0$ and $K_m(0, J-1) > 0$ with comparable magnitudes and $D_m(0, J-2) > 0$ but small, then $K_m(0, J) < K_m(0, J-2)$ by a small amount and $D_m(I, J) > D_m(I - 2m, J - 2)$ by a small amount. Thus, once this pattern is established, it must grow in amplitude so long as $K_0(I, J)$ remains slowly varying with I and the linearized equations are appropriate.

An example of this instability after it has grown very large is presented in Figs. 2a and b. In these figures a single mode is plotted over a limited range of v about $v = 0$ for two successive time (J) steps. Notice the large jump in amplitude and slope at $v = 0$ as predicted above. When this instability was encountered it was found to grow exponentially with a growth rate that was large enough to make it a serious problem.

In the Appendix a successful method for removing this instability is presented. The method is based on the assumption that $K_m(I + mJ, J) = G_m(I, J) + (-1)^J B_m(I, J)$, where $G_m(I, J)$ and $B_m(I, J)$ are smooth functions of I and J. It is a characteristic of the general numerical marching routine being presented here that the $K_m(I, J)$ are available for no more than two J values at any given integration step. In the Appendix it is shown that if the $G_m(I, J)$ and $B_m(I, J)$ are assumed second-order polynomials in $\Delta\tau$, then the $K_m(I, J)$ at two values of J are sufficient to individually determine the $G_m(I, J)$ and $B_m(I, J)$ for the two J values. Removal of the instability is accomplished by simply replacing the $K_m(I + mJ, J)$ by the $G_m(I, J)$ whenever the $B_m(I, J)$ are large enough to warrant doing so.

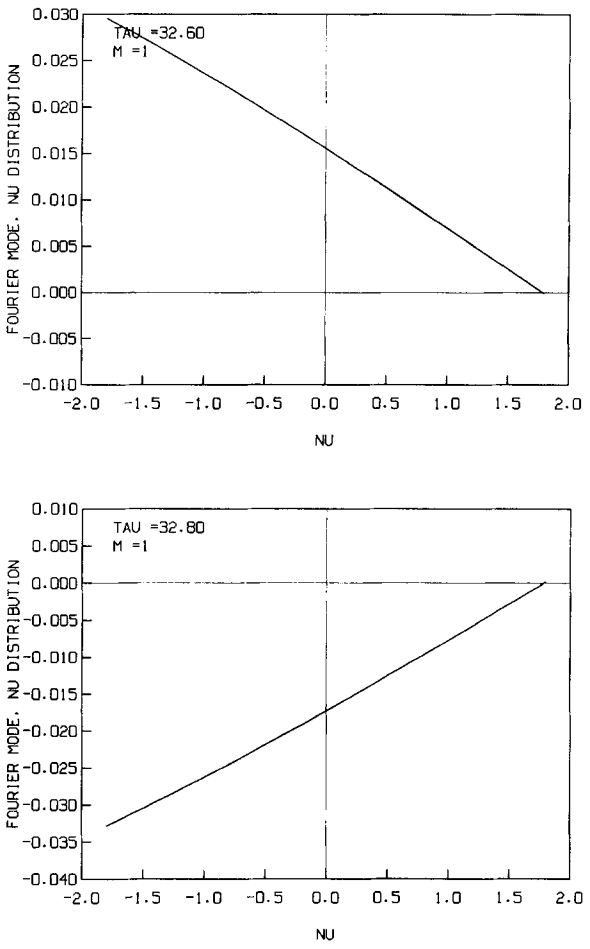

FIG. 2. A single mode at two successive time steps after the growth to very large amplitudes of the numerical instability discussed in Section Vb.

VI. RESULTS

The results to be presented here follow from considerations of three different initial plasma conditions. The first two of these have been considered before by Cheng and Knorr [13] and by many others before them who are referenced in their paper. No attempt will be made here to discuss the earlier results; those of Cheng and Knorr are the latest and are calculated using a numerical technique far removed from that used here. The third case presented here is based on actual electron observations in the earth's foreshock region. More details of the observation will be given shortly. The purpose of presenting this case is to demonstrate an application to the inter-

planetary plasma parameter regime. All three of these examples have periodic boundary conditions for which $\sigma_m(v, \tau) = 0$. In each case $M = 4$; nine field modes (including the space-averaged component) are included. This was the maximum number of modes considered during the development stage of this work. However, there is no inherent limitation to such a small number of modes in the computational method nor in the numerical code as it is written. In physical applications, especially those including nonperiodic solutions, larger numbers of modes will be included. In the last example presented here, where new physical phenomena have been discovered, the number of modes and the placement of the modes in wavelength have been varied to ensure that the results are not an artifact of the small number of modes.

The electric field is an important measurable property of the electrostatic plasma. It will be presented in terms of its Fourier series expansion,

$$\begin{aligned} E(x, \tau) &= E_0(\tau) + \sum_{m=1}^{M} [a_m(\tau) \cos(m\pi x) + b_m(\tau) \sin(m\pi x)] \\ &= E_0(\tau) + \sum_{m=1}^{M} [A_m(\tau) \cos m\pi(x + \varphi) + B_m(\tau) \sin m\pi(x + \varphi)], \end{aligned} \tag{28}$$

in which $E_0(\tau)$ is the space average of the electric field that Klimas [6] has shown can be calculated a priori:

$$E_0(\tau) = E_0(0) \cos(\tau) + (L/\lambda_D)\, u_0(0) \sin(\tau), \tag{29}$$

where $E_0(0)$ is an arbitrary constant which must be chosen as part of the initial data and where

$$u_0(0) = -\frac{i}{\pi} \frac{\partial K_0}{\partial v}\bigg|_{v=0, \tau=0}. \tag{30}$$

The coefficients in the Fourier series expansion are related to the solution of $K_m(v, \tau)$ through $b_m(\tau) = B_m(\tau) \cos m\pi\phi(\tau) - A_m(\tau) \sin m\pi\phi(\tau)$ and $a_m(\tau) = A_m(\tau) \cos m\pi\phi(\tau) + B_m(\tau) \sin m\pi\phi(\tau)$ in which

$$A_m(\tau) = -(\gamma/m)\, \mathrm{Im}\, K_m(0, \tau) \tag{31-a}$$

and

$$B_m(\tau) = -(\gamma/m)\, \mathrm{Re}\, K_m(0, \tau). \tag{31-b}$$

Here $\gamma = 2L/\pi\lambda_D$,

$$\varphi(\tau) = \frac{\lambda_D}{L} \int_0^\tau d\lambda (\tau - \lambda)\, E_0(\lambda), \tag{32}$$

L is an arbitrary length scale over which the dimensional position variable x is

measured, and λ_D is the Debye length. The actual Fourier coefficients are a time dependent superposition of $A_m(\tau)$ and $B_m(\tau)$ which depends on the constants $E_0(0)$ and $u_0(0)$. In order to avoid the extra degree of freedom involved in the choice of the constant $E_0(0)$, the results for the electric field will be presented here in terms of the $A_m(\tau)$ and $B_m(\tau)$. In the special case when $E_0(0) = u_0(0) = 0$, then $E_0(\tau) = 0$ and the electric field given by Eq. (28) reduces to the electrostatic approximation. In this case solutions of the generalized electron plasma model considered here can be compared directly with other solutions of the electrostatic Vlasov–Poisson system. In the first two examples to follow, $E_0(0)$ has been set to zero as part of the initial data and initial velocity distributions are chosen which are symmetric in velocity; therefore $u_0(0) = 0$.

A. *Nonlinear Landau Damping*

In this case, in terms of the dimensionless variables used by Klimas [6], the initial velocity distribution is given by

$$F(x, v, 0) = \sqrt{2\pi}(1 - \cos \pi x) \exp[-\tfrac{1}{2}(2\pi v)^2].$$

After the Fourier–Fourier transformation, the initial data are given by $K_0(v, 0) = \exp[-\frac{1}{2}(v/2)^2]$, $K_1(v, 0) = K_{-1}(v, 0) = -\frac{1}{4}K_0(v, 0)$, and all other $K_m(v, 0) = 0$. Because of the symmetry of the initial data in v, $u_0(0) = 0$. If $E_0(0)$ is assumed equal to zero, the system of equations considered by Klimas [6] reduces to that considered by Cheng and Knorr [13] and since the initial data for their "strong nonlinear Landau damping" example is identical to that used here, the results can be compared directly.

Figures 3a–d should be compared to Fig 4 of Cheng and Knorr. Notice that there

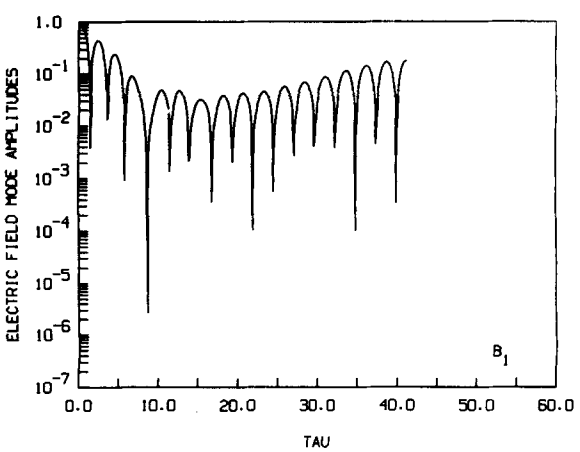

FIG. 3. Nonlinear Landau damping: the absolute values of the electric field Fourier coefficients as functions of τ. If a coefficient reaches 1, then the field energy density in that mode is equal to the initial thermal energy of the electron plasma.

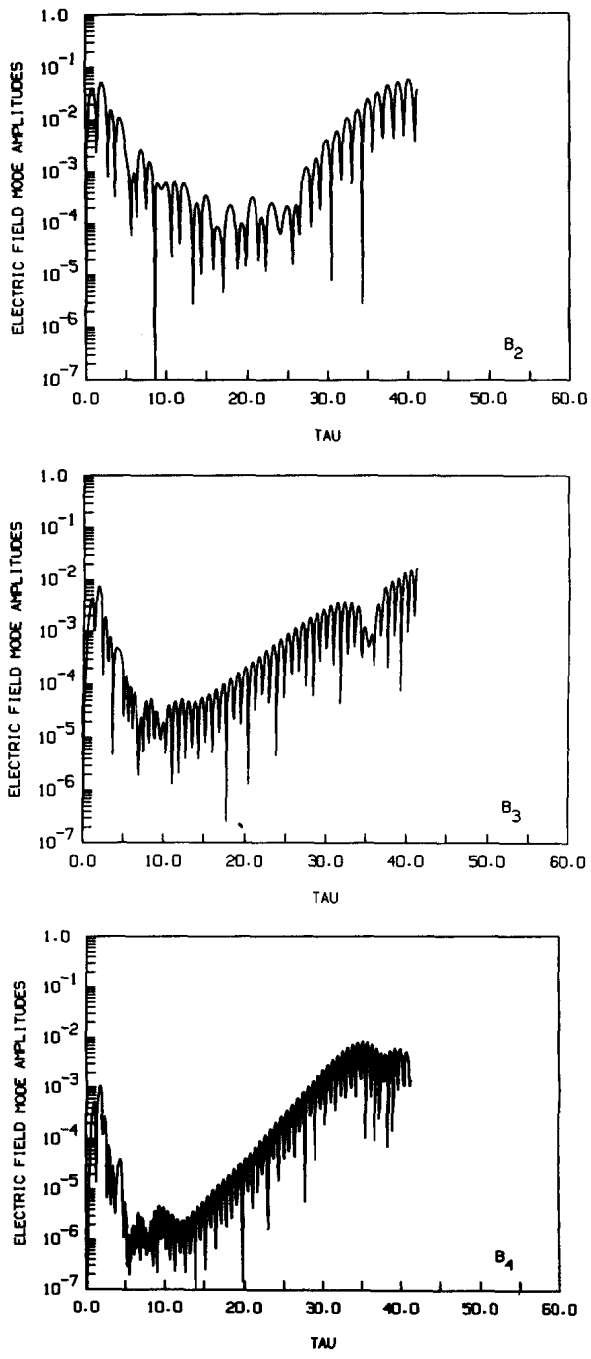

FIGURE 3 *(continued)*

is a constant scaling factor of two in going from the E_m of Cheng and Knorr to the B_m in Figures 3a–d. The results for the dominant first mode are in excellent agreement and even the smaller second mode results contain only minor differences. The third mode results are only qualitatively similar, but the third mode is also very small contribution to the total electric field.

In their Fig. 5, Cheng and Knorr have plotted the space-averaged velocity distribution at various instants in time. With the Fourier–Fourier transform approach taken here the velocity distribution, of course, is not directly available. However, a fast Fourier transform routine has been applied to $K_0(v, \tau)$ to invert the Fourier transformation in velocity space and thereby obtain the space-averaged velocity distribution for comparison with Cheng and Knorr. Some results of this inversion are given in Figs. 4a and b for two times which are also presented by Cheng and Knorr.

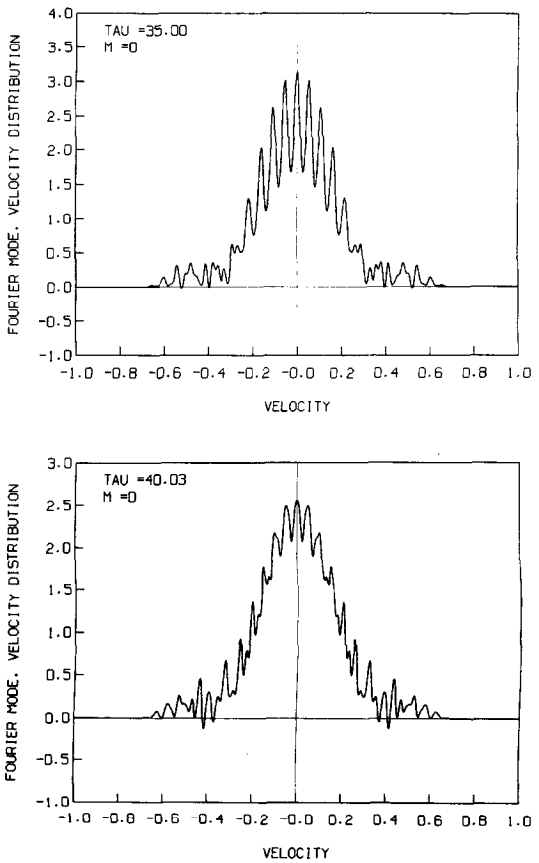

FIG. 4. Nonlinear Landau damping: the space average of the electron velocity distribution at two instants in time. Slight negative excursions are errors due to the truncation of the Fourier series expansion of the electron distribution function at a finite number.

The comparison at $\tau = 35$ is excellent with only minor differences in the results in the low amplitude, large velocity tails on the distribution. The comparison for all earlier times is equally good or better. Considering the vastly different types of approaches which have been taken to obtain this comparison, the excellent agreement which is obtained has to be taken as a verification of both approaches.

The comparison at $\tau = 40$ is not quite as good. The velocity-space filamentation which has been developing up to this time seems to largely vanish in the results of Cheng and Knorr but it does not vanish at all in the results obtained here. Perhaps the recurrence effect in the method of Cheng and Knorr is responsible, but this is only a guess. There does not seem to be any reason to expect the filamentation to vanish after it has formed.

Figures 5 and 6 show the development of $K_{-4}(v, \tau)$ for this Landau damping case. Figure 5 is characteristic of damping evolution. The entropy density in the mode propogates away from the line $v = 0$ along the characteristic direction of the mode (in this case $v = v_0 - 4\tau$) leaving the amplitude of the mode at $v = 0$ smaller with increasing τ. Figure 6 shows the same mode at a later time. The dominant feature in this figure is still the large amplitude wave train propagating along the characteristic direction. This propagation along the characteristics to large v-values allows for fine structure in the corresponding velocity distribution; i.e., velocity filamentation. Thus, Landau damping should be expected to lead to severe velocity-space filamentation. The reversal of the decay of the electric field modes which is evident in Fig. 3a–d is due to the growth of the very regular waves in the vicinity of and to the right of $v = 0$ in Fig. 6. Because of the growth of these waves and the simultaneous spreading of the solution to large v values, this case became very difficult to calculate. From $\tau \simeq 15$ to the end of the run both v_{max} and λ_{max} grew with increasing τ leading to four halvings

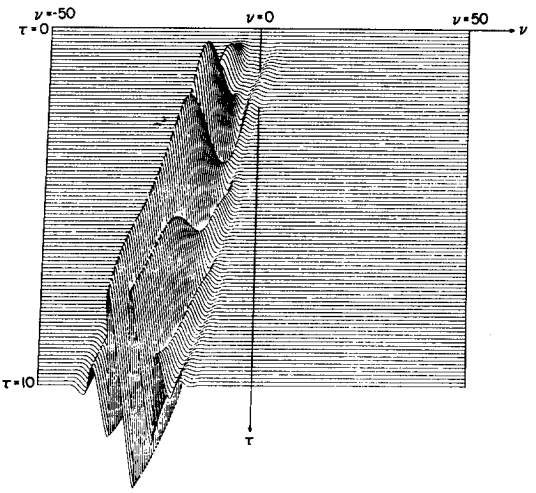

FIG. 5. Nonlinear Landau damping: real part of $K_{-4}(v, \tau)$ for small τ showing initial damping stage. Notice that τ increases from "back to front" of drawing; $m = -4$ mode, $M = 4$.

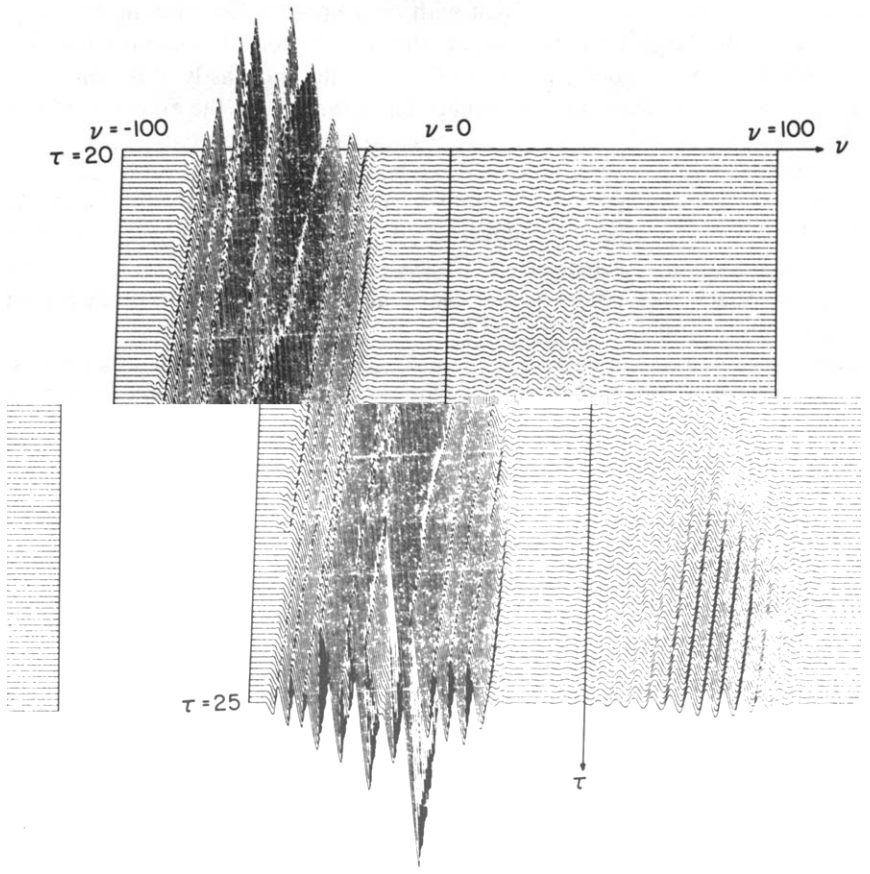

FIG. 6. Nonlinear Landau damping: real part of $K_{-4}(v, \tau)$ for τ much larger than in Fig. 5 showing damping reversal; $m = -4$ mode, $M = 4$.

of the grid spacing. The combination of the grid spacing halvings plus the overall growth of the size of the domain on which the calculation was being done made further progress impractical. The difficulty is due directly to the entropy conservation requirement. If this requirement were relaxed, then the very large v_{max} and the related grid spacing halvings would not be required but the accuracy of the resulting solution would be in question.

B. *Two-Stream Instability*

The second comparison with the results of Cheng and Knorr which is presented here shows the evolution of a two-stream instability. In this case the initial velocity distribution is given by

$$F(x, v, 0) = \sqrt{2\pi}(1 - .05 \cos \pi x)(2\pi v)^2 \exp[-\tfrac{1}{2}(2\pi v)^2].$$

The initial data for the Fourier–Fourier transformed variables is given by

$$K_0(v, 0) = [1 - (v/2)^2] \exp[-\tfrac{1}{2}(v/2)^2],$$
$$K_1(v, 0) = K_{-1}(v, 0) = -.025K_0(v, 0),$$

and all other $K_m(v, 0) = 0$.

The electric field mode amplitudes are plotted in Figs. 7a–d; they should be compared with the results of Cheng and Knorr for these quantities in their Fig. 6. Again, a quantitative comparison of the results for the dominant first mode indicates excellent agreement. The higher modes are in excellent agreement only for short times and agree only qualitatively for longer times. Perhaps the differences in detail that do exist are due to the small number of modes that are included in the results here.

Figures 8 and 9 are included to show the very different kind of evolution which occurs during the growth and saturation of an instability such as this one. In Fig. 8 notice the increase in amplitude which occurs in the vicinity of $v = 0$ as τ increases. [illegible] preclude propagation away from $v = 0$. Indeed, in Fig. 9 the same mode is shown over an interval of τ when saturation of the instability has already taken place. Notice that the solution has not spread significantly in v beyond that which occurred much earlier and that there is no evidence for further spreading. In this case there does not seem to be a basis for significant velocity-space filamentation because the solution is negligibly small at large values of v for all modes. In fact, the space-averaged velocity distribution shown in Fig. 10 for $\tau = 40$ shows very little evidence of filamentation. Cheng and Knorr made the same observation in their discussion of this two-beam instability. Because there was no significant spreading in this solution, the calculation

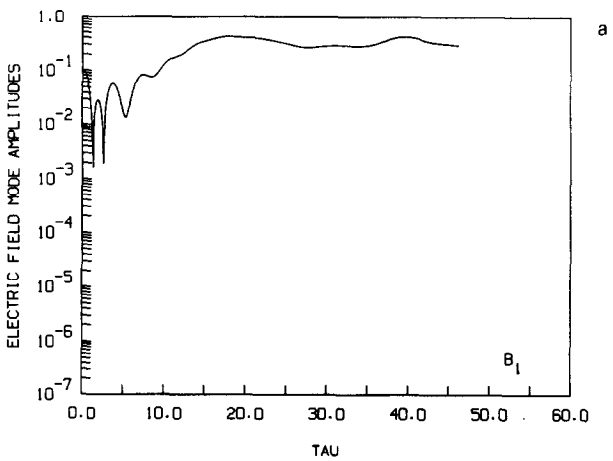

FIG. 7. Two-beam instability: same as Fig. 3.

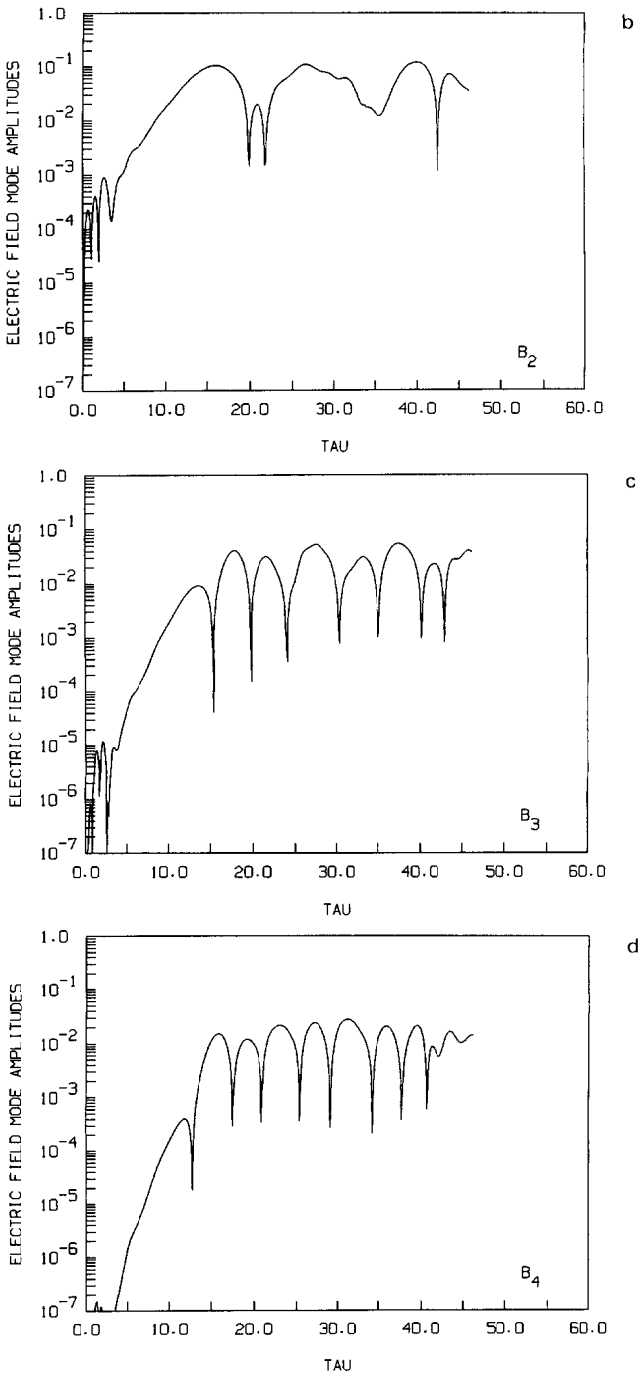

FIGURE 7 *(continued)*

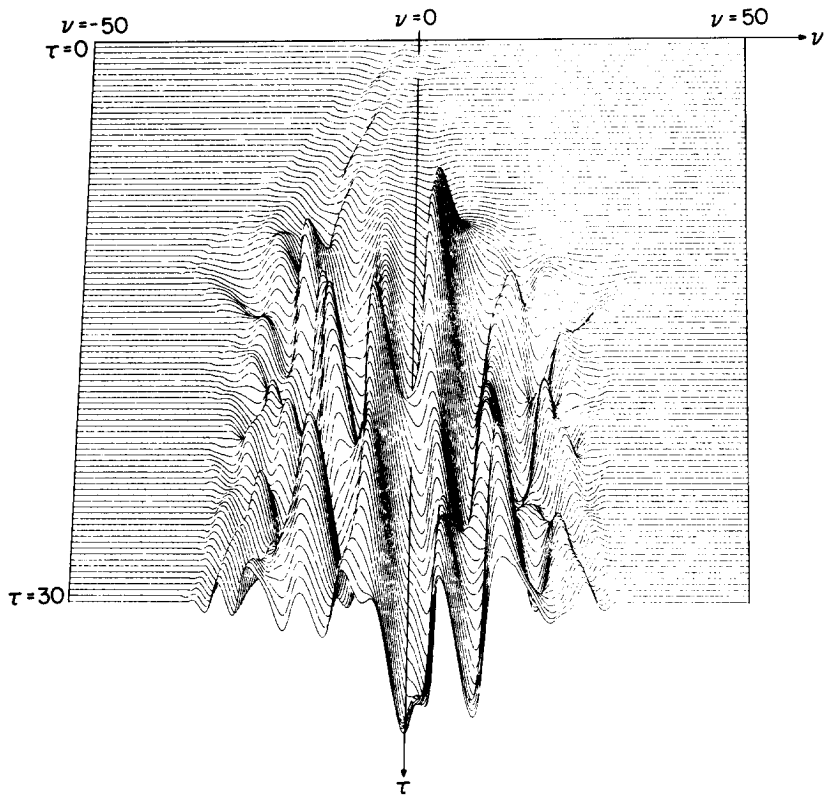

FIG. 8. Two-beam instability: real part of $K_{-2}(v, \tau)$ for small τ showing initial growth of instability; $m = -2$ mode, $M = 4$.

went quickly with only one halving of the grid spacing. The run was stopped when essential agreement with the results of Cheng and Knorr had been demonstrated; in contrast with the Landau damping example discussed above, there was no reason for not continuing if it were desired. Within the Fourier–Fourier transform technique, as higher modes are added the potential for more rapid spreading of the solution is increased. However, for this two-stream instability it was found that the spreading was essentially unaffected by the number of modes included. Thus, an extension of this calculation to many more modes seems promising.

C. *Bump-on-tail Instability*

The dots in Fig. 11 represent GSFC electron spectrometer data taken aboard the ISEE-1 spececraft on November 6, 1977, at 11:38:13 UT when the spacecraft was experiencing strong electrostatic turbulence in the foreshock region of the Earth's bow shock. The solid curve is a three-Gaussian fit to the data which was used for the initial velocity distribution for the numerical integration to be presented in this

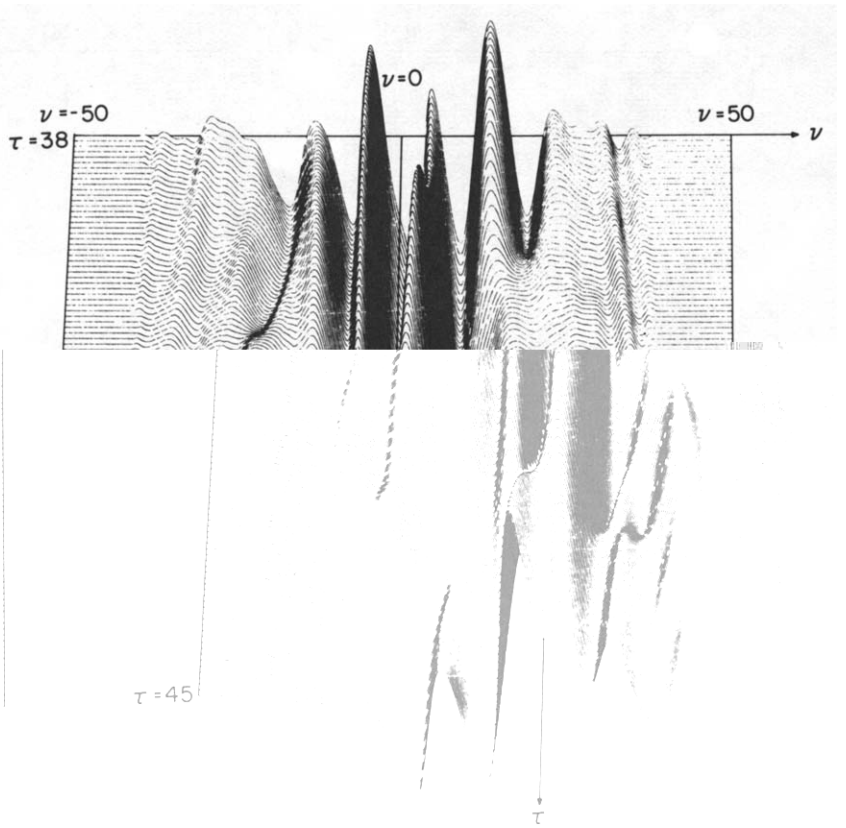

FIG. 9. Two-beam instability: real part of $K_{-2}(v, \tau)$ showing saturation of the instability; $m = -2$ mode, $M = 4$.

section. All modes were given the same initial velocity distribution but the amplitudes of the modes with $m \neq 0$ were set at 10^{-6} of the amplitude of the mode with $m = 0$. Here $E_0(\tau)$ cannot be assumed zero because $u_0(0)$, which is determined by the initial data, is not zero. Thus, this example cannot be calculated in the electrostatic approximation using the Vlasov–Poisson system of equations. The nonsymmetric nature of the observed electron data makes the reduction to that approximation impossible. The full expression given by Eq. (28) must be used to calculate the electric field, and the conservation laws for reduced momentum and energy are no longer for physical quantities. For the results to be discussed in this section the change in reduced momentum was approximately 0.05% of the original, the change in reduced energy 0.3% of the original, and for entropy, 0.04% of the original.

The thin vertical lines in Fig. 11 represent the initial phase velocities of the electric field modes. Analysis of a linearized version of the equations being considered here indicates that the mode with phase velocity which lies on that part of the "bump" on the initial velocity distribution with positive slope should be unstable; i.e., while it,

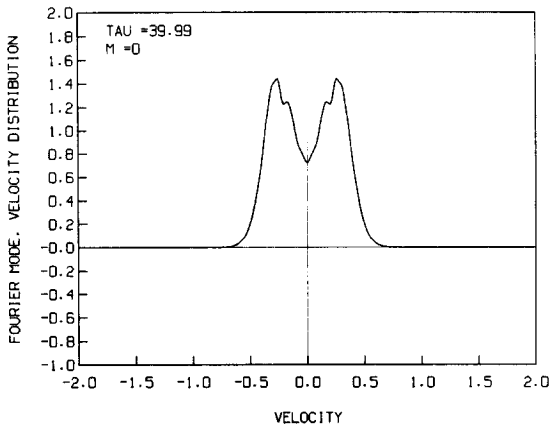

FIG. 10. Two-beam instability: the space average of the electron velocity distribution function following saturation of the instability. Note the persistence of the two beams and the lack of strong velocity space filamentation.

and all the other modes, oscillate harmonically at their respective Bohm–Gross frequencies, its amplitude should grow exponentially in time with a growth rate than can be predicted. According to this analysis the amplitudes of all other modes in this example should decay exponentially with various rates.

Figures 12a–d contain the B_m's for this run. The A_m's will not be presented since they are qualitatively the same as the B_m's. The second mode, $B_2(\tau)$, is the mode which is expected to grow exponentially; it does initially with a growth rate close to that predicted by the linear analysis. The remaining modes decay initially as expected. The reversal of the decay of $B_4(\tau)$ with an increase in its oscillation frequency by roughly a factor of two was not expected. This is the first time that this phenomenon has been found in a calculation of the bump-on-tail plasma instability. The number of modes in this calculation as well as their placement in phase velocity

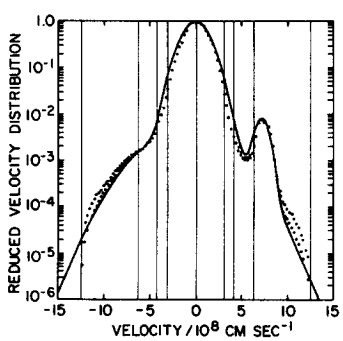

FIG. 11. Bump-on-tail instability: fit (solid curve) to ISEE-1 electron spectrometer data (dots) used for initial condition. Uncertainty in the data is indicated by spread in dots.

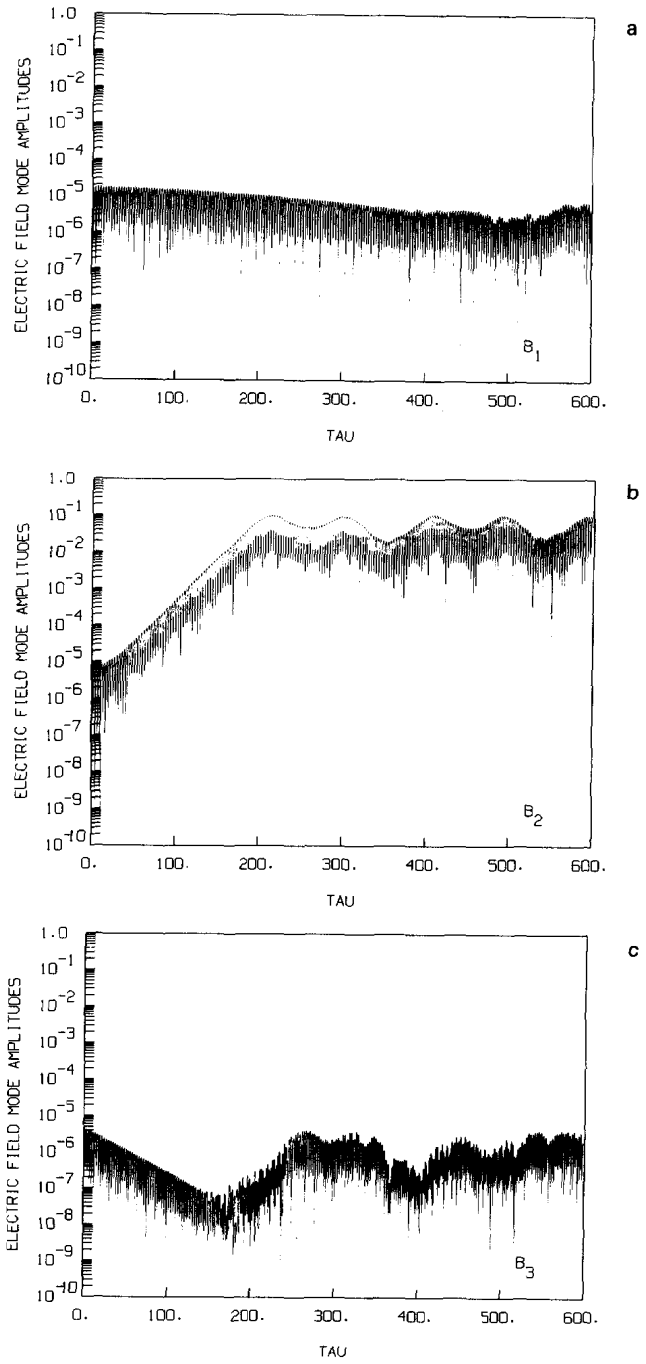

FIG. 12. Bump-on-tail instability: same as Fig. 3.

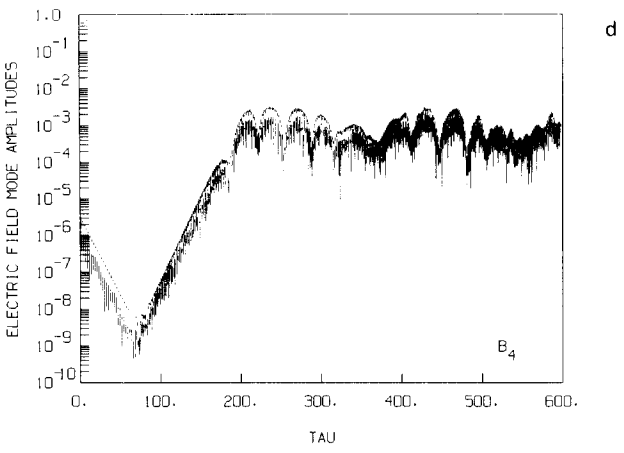

FIGURE 12 *(continued)*

has been varied to ensure the correctness of this result. Standard tests like halving the grid spacing or varying parameters which govern the number of iterations, and therefore the accuracy of the solution, were applied with no change in the results. Oscillations in the electric field at twice the plasma frequency have been observed aboard the ISEE-1 spacecraft but, for theoretical reasons, have been assumed either experimental error or electromagnetic in origin. On the other hand, there is no experimental evidence at present that these oscillations are electromagnetic and there is growing evidence that the harmonic detections are real [25].

Figures 13a–f give an indication of the time evolution of the space average of the velocity distribution function late in the numerical run. At $\tau = 170$ the distribution is still essentially the initial distribution. As the growing electric field modes approach saturation, the dip in the velocity distribution between the central Gaussian and the bump begins to fill in. At $\tau \simeq 210$, when the electric field reaches its first maximum, the bump has been reduced to a plateau with some weak velocity space filamentation superimposed. However, later whenever the field strength reduces, the bump reappears. This phenomenon may be due to the small number of modes included in the calculation but tests of this conjecture have not been conclusive. For example, a run was made in which only three field modes were included but the integration went to $\tau \gtrsim 1000$. In that case the oscillatory reappearance of the bump was initially stronger but the oscillations decayed away by $\tau \simeq 500$. When a larger number of modes have been included the oscillations have been found initially weaker but they have shown no tendency to decay away. The weak velocity space filamentation in the vicinity of the bump may also be due to the small number of modes. But, no tendency for these waves to disappear with an increase in the number of modes has been found. Confirmation of the reality of these waves must await further computations with more modes included and/or a calculation by an independent investigator using the same initial conditions.

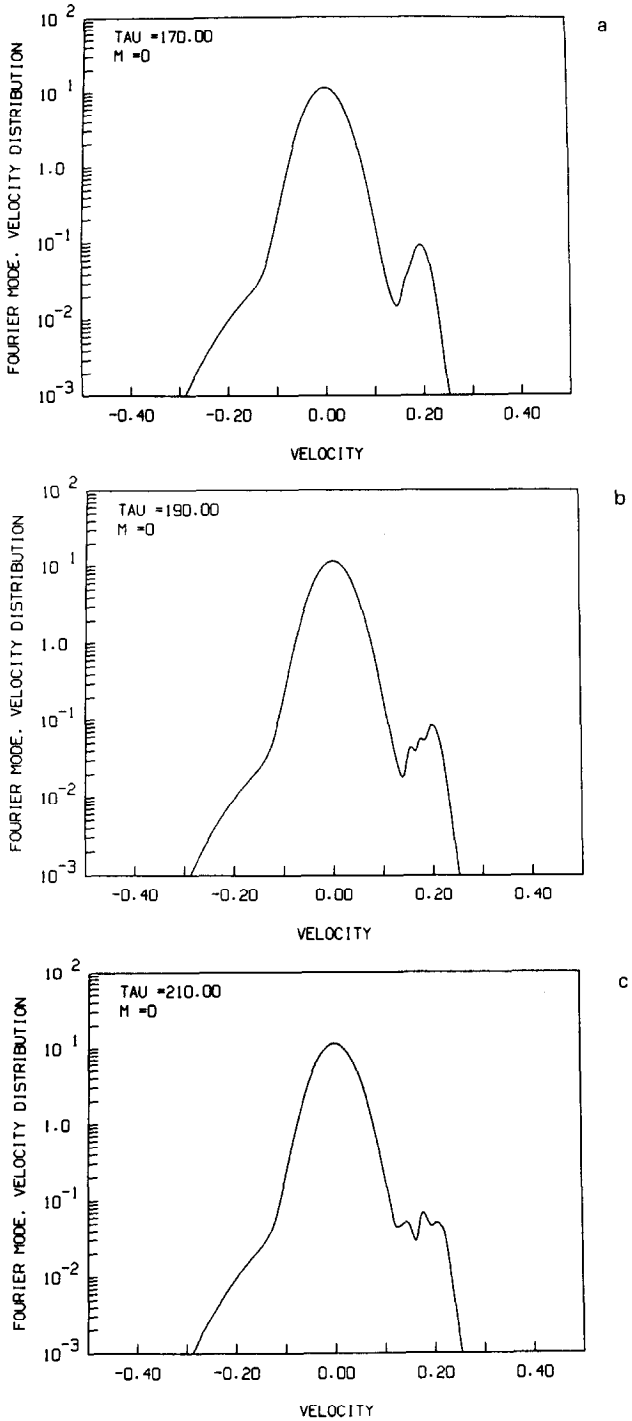

FIG. 13. Bump-on-tail instability: the space average of the electron velocity distribution functions as the instability saturates. Note the reappearance of the bump after the overshoot in the dominant electric mode shown in Fig. 12b.

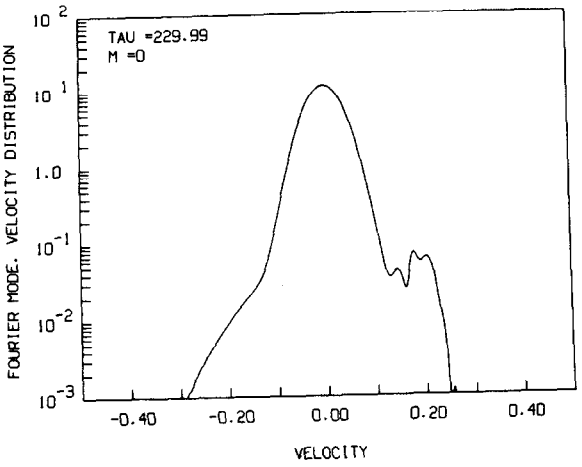

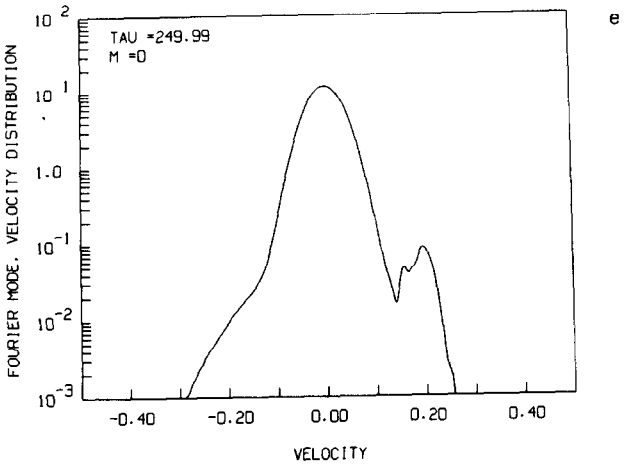

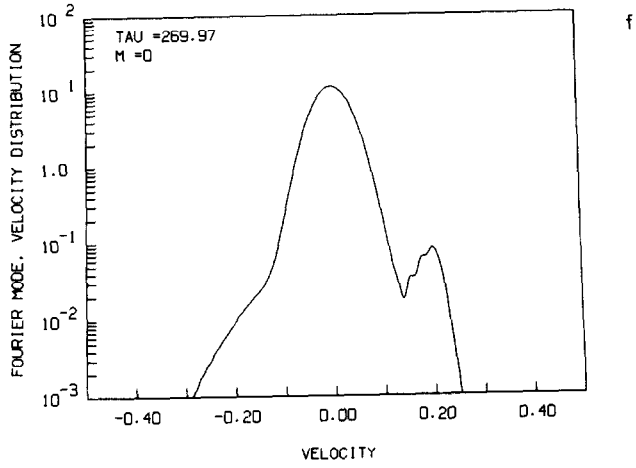

FIGURE 13 *(continued)*

Figures 14 and 15 are plots of the contrasting early evolution of the real parts of $K_{-2}(v, \tau)$ and $K_{-4}(v, \tau)$. Both modes contain a wave train propagating away from the origin along their respective characteristic directions in a manner similar to the earlier Landau damping example. Both modes also contain a string of pulsations in the vicinity of $v = 0$. But, for $m = -4$ these pulsations decay as τ increases, thereby leading to the initial decay phase of $B_4(\tau)$ (and $A_4(\tau)$ as well). These pulsations in $K_{-2}(v, \tau)$ grow with increasing τ but, interestingly, nothing else happens. At saturation, shown in Fig. 16, $K_{-2}(v, \tau)$ still contains the same string of pulsations near $v = 0$ with the same shape and frequency but with a much larger amplitude. The growth of this remarkably stable waveform is responsible for the exponential rise in $B_2(\tau)$ (and $A_2(\tau)$) shown in Fig. 12b. Figure 17 contains a plot of $K_{-4}(v, \tau)$ over a

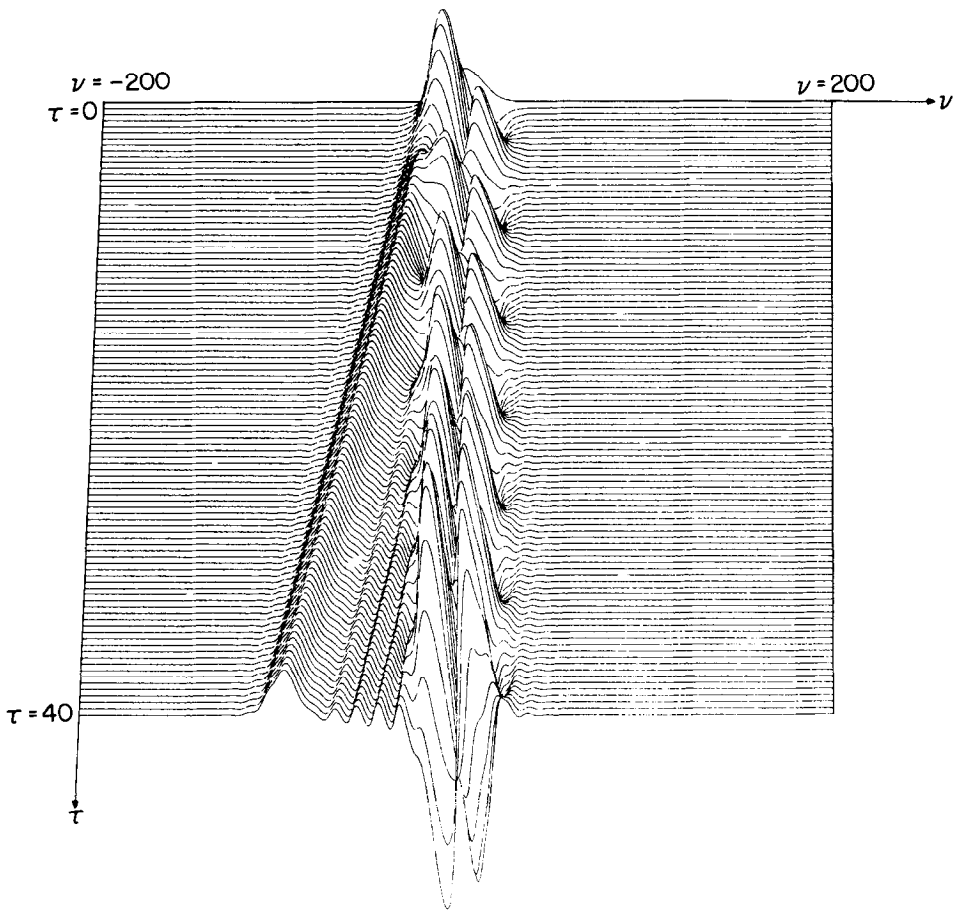

FIG. 14. Bump-on-tail instability: real part of $K_{-2}(v, \tau)$ for small τ showing initial growth of pulsation near $v = 0$; $m = -2$ mode, $M = 4$.

time interval just after the reversal of the decay of $B_4(\tau)$ (and $A_4(\tau)$). The wave train characteristic of Landau damping continues to propagate away from the $v = 0$ line along this mode's characteristic direction but the growth of some small regular waves in the vicinity of $v = 0$ is evident. These waves are responsible for the decay reversal. Notice the strong similarity between the behavior of this mode with the behavior of $K_{-4}(v, \tau)$ shown in Figs. 5 and 6 for the Landau damping example.

The mechanism for the excitation of the second harmonic oscillations is relatively easy to understand. It appears that this mechanism may operate in many situations in interplanetary plasmas. The critical elements of this mechanism are the initial low

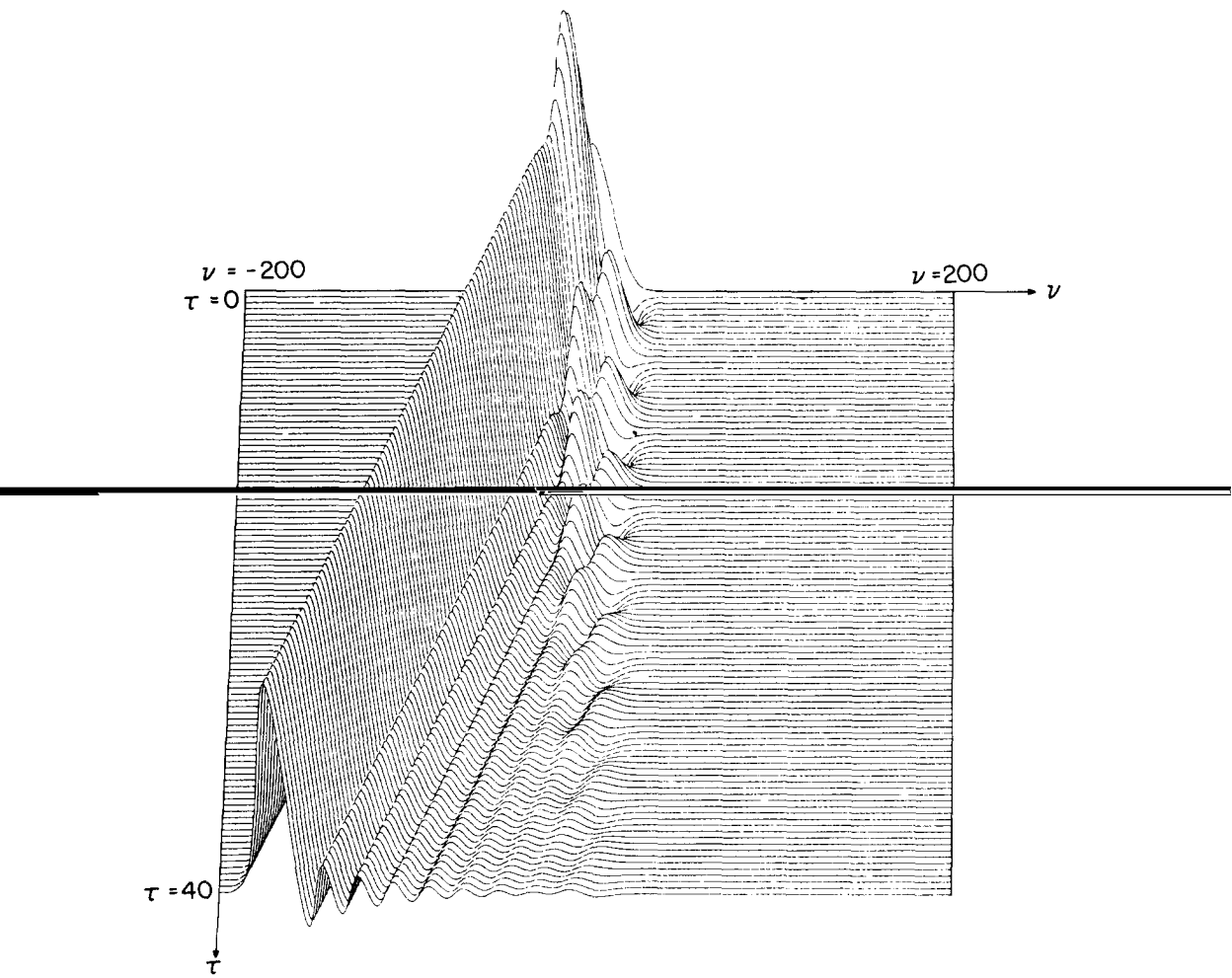

FIG. 15. Bump-on-tail instability: real part of $K_{-4}(v, \tau)$ for small τ showing initial decay of pulsations near $v = 0$; $m = -4$ mode, $M = 4$.

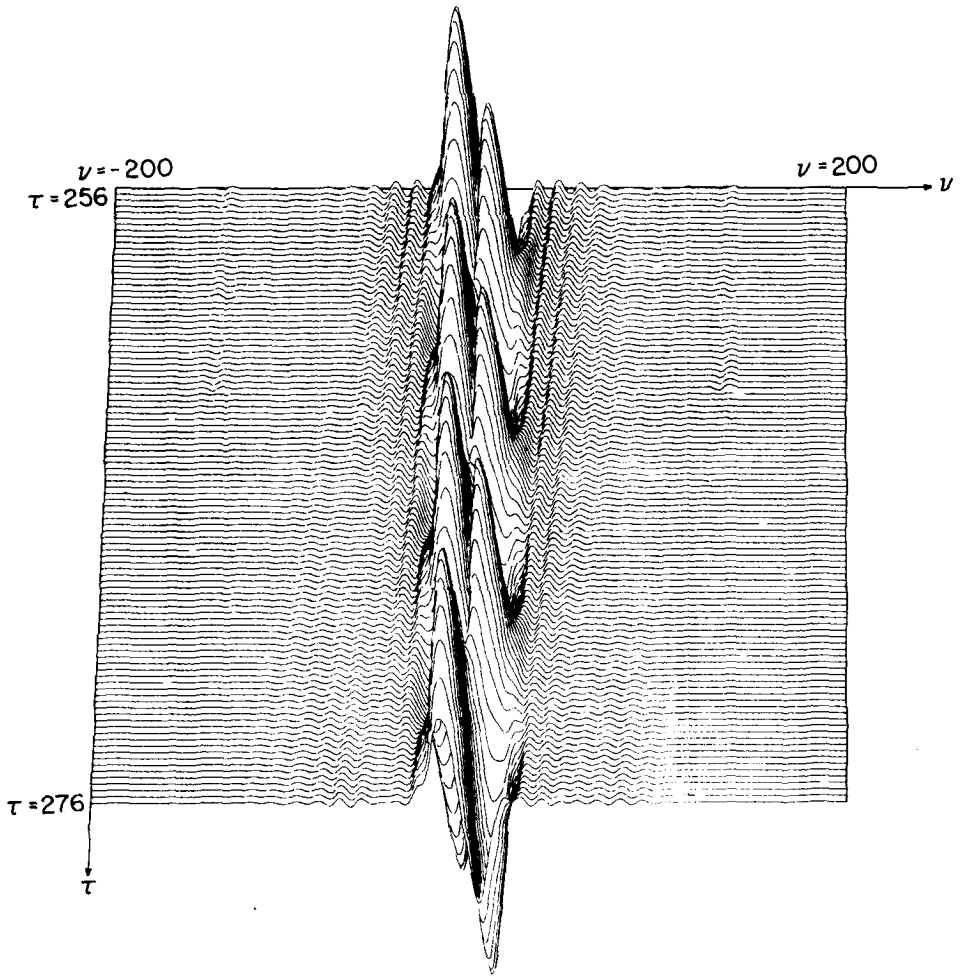

FIG. 16. Bump-on-tail instability: real part of $K_{-2}(v, \tau)$ for large τ showing details of pulsations near $v = 0$ after saturation of the instability; $m = -2$ mode, $M \simeq 4$.

level of the field modes before the excitation of the instability plus the small growth rate of the instability. Then the linear growth phase of the instability lasts long enough for the amplitudes of the growing mode(s) and the decaying modes to move so far apart that the linear plasma theory, which would not allow the second harmonic excitation, becomes misordered. Quadratic terms in the growing field modes actually dominate over linear terms in the decaying modes. A form of second-order wave–wave coupling [26] takes over which allows the unstable modes to pump the decaying modes. The pumped mode must grow with twice the growth rate and it

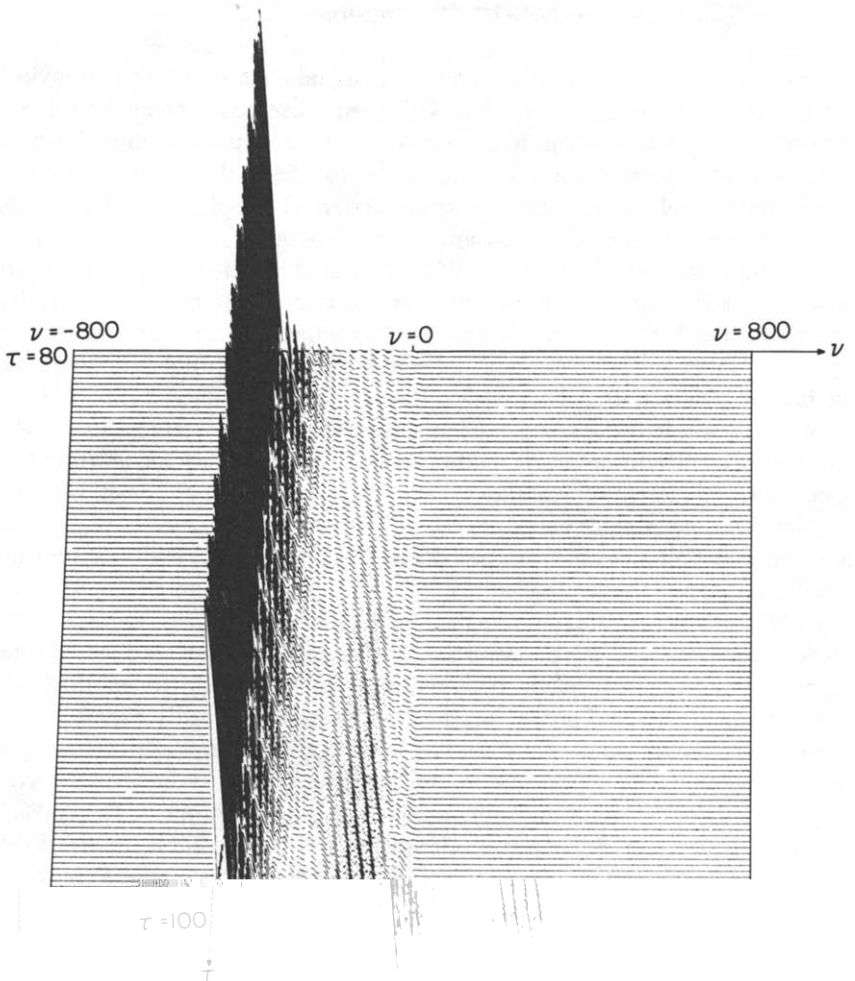

FIG. 17. Bump-on-tail instability: real part of $K_{-4}(v, \tau)$ showing the reversal of the decay of this mode at $v = 0$, $m = -4$ mode, $M = 4$.

must oscillate with twice the oscillation frequency of the unstable mode. These are properties of $B_4(\tau)$ following the reversal of its linear decay when compared to the unstable $B_2(\tau)$. Notice that, at $\tau \simeq 70$, just as the growth $B_4(\tau)$ begins its amplitude is comparable to the square of the amplitude of $B_2(\tau)$. Further numerical runs which are being carried out as this is being written show that higher harmonics are also excited through this mechanism. A quantitative study of this mechanism is in progress and will appear later.

VII. Conclusion

A numerical method for modeling one-dimensional electron plasma behavior under typical interplanetary plasma conditions has been presented. The method is based on the Fourier–Fourier transform technique applied to a plasma model which is a generalization of the electrostatic plasma equations; the evolution of a nonzero space-averaged electric field is included. A construction of the discretized equations has been given along with a brief discussion of the associated discretization error. It has been shown that this error is formally fifth order in the grid spacing but this ordering has also been shown to be nonuniform over the grid. A method for controlling this nonuniformity has been introduced. This method allows for a larger grid spacing than was possible in earlier approaches to the nonuniformity problem. Several conservation laws which are used to test the accuracy of the numerical integration have been discussed. Three of these have been shown to be closely related to conservation laws in the electrostatic limit. An additional conservation law for entropy has been included. Two numerical instabilities have been identified and methods for their suppression have been presented.

Three examples of plasma evolution have been presented. The first two of these have been compared to the earlier results of Cheng and Knorr [13] who used an entirely different method to obtain them. The comparison verifies the results of Cheng and Knorr and establishes the accuracy of the method presented here. The third example that has been presented demonstrates an application to an ISEE electron observation made in the Earth's foreshock. The results of this example are quite surprising. It has been found that during the linear growth phase of this bump-on-tail instability, one of the stable modes become pumped through a quadratic wave–wave interaction with the dominant unstable mode. The pumped mode shifts its oscillation frequency to twice the Bohm–Gross frequency of the unstable mode. Following saturation the electric field is dominated by plasma oscillations at the basic Bohm–Gross frequency of the unstable mode and its second harmonic. This kind of behavior has not been associated before with bump-on-tail evolution. An explanation for the second harmonic excitation has been given which shows that its occurrence is due to the interplanetary plasma state used for the initial conditions in the numerical integration. It has been shown that second and higher harmonic excitation may be a common occurrence in interplanetary plasma. These results have led to a reexamination of several assumptions which have been made concerning the ISEE data. This reexamination is in progress; conclusions will be presented elsewhere.

In the future, solutions with nonperiodic boundary conditions will be studied by including $\sigma(v, \tau) \neq 0$. In the third example that has been presented here, the evolution of a bump-on-tail instability has been examined, given that the bump on the velocity distribution has been found to exist. Of further physical importance is an answer to the question "How did the bump get generated in the first place?" Nonperiodic boundary conditions must be added in order to approach thus question.

APPENDIX

In Section Vb it was shown that Eqs. 4–8 are unstable when the electric field modes are very small and the $K_0(I, J)$ mode is slowly varying with I. Some results of allowing this instability to grow unchecked were also presented there. The results in Section VI for the bump-on-tail (physical) instability were obtained only after the growth of this numerical instability was prevented. In this appendix the method used for preventing that growth is presented.

Consider Eqs. (4)–(8) with the change of notation given by $K_m(I, J) = h_{m+M+1}(I, J)$ with $-M \leqslant m \leqslant M$. Suppose the $K_m(I, J)$ are known for two successive values of J which will be arbitrarily labeled here as $J = 0$ and $J = 1$. Let $F_m(I, J) = K_m(I + mJ, J)$. Then, from Eqs. (4)–(8),

$$\begin{aligned} F_m(I, 2) = F_m(I, 0) + (\varepsilon/(m-n))[&(I + 2m) F_{m-n}(-2(m-n), 2) F_n(I + 2(m-n), 2) \\ &+ 4(I + m) F_{m-n}(-(m-n), 1) F_n(I + (m-n), 1) \\ &+ I F_{m-n}(0, 0) F_n(I, 0)] \end{aligned} \tag{A1}$$

in which the sum over n with $n \neq m$ and $|n| \leqslant M$ is implied. Now assume that the $F_m(I, J)$ are a mixture of good plus bad data given by $F_m(I, J) = G_m(I, J) + (-1)^J B_m(I, J)$ with

$$G_m(I, J) = G_m(I) + (J\Delta\tau)\,\alpha_m(I) + (J\Delta\tau)^2 \beta_m(I) \tag{A2}$$

and

$$B_m(I, J) = B_m(I) + (J\Delta\tau)\,\gamma_m(I) + (J\Delta\tau)^2\,\delta_m(I) \tag{A3}$$

The $G_m(I, J)$ are the components of the instability-free solution to Eq. (A1) which is to be found. Thus, the $G_m(I, J)$ must be the solution of Eq. (A1) with the $B_m(I, J) = 0$. Bu substituting Eq. (A2) into Eq. (A1) and then equating coefficients of equal powers of $\Delta\tau$, the $\alpha_m(I)$ and $\beta_m(I)$ can be calculated in terms of the $G_m(I)$. This substitution must be carried out with care, however, because of the explicit appearance in Eq. (A1) of the index I which takes on large values of $O(\Delta\tau^{-1})$ on the domain of this calculation. Thus, over this domain $\varepsilon I = \frac{1}{3} v\,\Delta\tau$ must be treated as $O(\Delta\tau)$. With this proviso the calculation is straightforward and yields,

$$\begin{aligned} \alpha_m(I) = \frac{1}{6}\left(\frac{v}{m-n}\right)[&G_{m-n}(-2(m-n))\, G_n(I + 2(m-n)) \\ &+ 4G_{m-n}(-(m-n))\, G_n(I + (m-n)) + G_{m-n}(0)\, G_n(I)] \end{aligned} \tag{A4}$$

and

$$\begin{aligned}\beta_m(I) = \frac{1}{6}\left(\frac{v}{m-n}\right)[&G_{m-n}(-2(m-n))\,\alpha_n(I+2(m-n))\\&+\alpha_{m-n}(-2(m-n))\,G_n(I+2(m-n))\\&+2G_{m-n}(-(m-n))\,\alpha_n(I+(m-n))+2\alpha_{m-n}(-(m-n))\,G_n(I+(m-n))]\\&+\frac{1}{6}\left(\frac{m}{m-n}\right)[G_{m-n})-2(m-n))\,G_n(I+2(m-n))\\&+2G_{m-n}(-(m-n))\,G_n(I+(m-n))].\end{aligned}\tag{A5}$$

The $B_m(I,J)$ will be assumed small compared to the $G_m(I,J)$ for all values of m. Thus, a linearized version of Eq. (A1) can be constructed in which all terms containing powers of the $B_m(I,J)$ higher than first are neglected. Then, a calculation for the $B_m(I,J)$ similar to the one described above for the $G_m(I,J)$, but this time using this linearized equation, can be carried out to relate the $\gamma_m(I)$ and $\delta_m(I)$ to the $G_m(I)$ and $B_m(I)$. The results are,

$$\begin{aligned}\gamma_m(I) = \tfrac{1}{6}(v/(m-n))[&G_{m-n}(-2(m-n))\,B_n(I+2(m-n))\\&+B_{m-n}(-2(m-n))\,G_n(I+2(m-n))\\&-4G_{m-n}(-(m-n))\,B_n(I+(m-n))\\&-4B_{m-n}(-(m-n))\,G_n(I+(m-n))\\&+G_{m-n}(0)\,B_n(I)+B_{m-n}(0)\,G_n(I)]\end{aligned}\tag{A6}$$

and

$$\begin{aligned}\delta_m(I) = \tfrac{1}{6}(v/(m-n))[&\alpha_{m-n}(-2(m-n))\,B_n(I+2(m-n))\\&+G_{m-n}(-2(m-n))\,\gamma_n(I+2(m-n))\\&+\gamma_{m-n}(-2(m-n))\,G_n(I+2(m-n))\\&+B_{m-n}(-2(m-n))\;\alpha_n(I+2(m-n))\\&-2\alpha_{m-n}(-(m-n))\,B_n(I+(m-n))\\&-2G_{m-n}(-(m-n))\,\gamma_n(I+(m-n))\\&-2\gamma_{m-n}(-(m-n))\,G_n(I+(m-n))\\&-2B_{m-n}(-(m-n))\,\alpha_n(I+(m-n))]\\&+\tfrac{1}{6}(m/(m-n))[G_{m-n}(-2(m-n))\,B_n(I+2(m-n))\\&+B_{m-n}(-2(m-n))\,G_n(I+2(m-n))\\&-2G_{m-n}(-(m-n))\,B_n(I+(m-n))\\&-2B_{m-n}(-(m-n))\,G_n(I+(m-n))]\end{aligned}\tag{A7}$$

Thus, with this approach it is possible to construct an expression for $F_m(I, J)$ which has only two independent vector quantities, $G_m(I)$ and $B_m(I)$, for each value of the index I. It is further possible to calculate the $G_m(I)$ and $B_m(I)$ in terms of the $F_m(I, 0)$ and $F_m(I, 1)$ which are known. This calculation is outlined in the following:

When $J = 0$,

$$K_m(I, 0) = G_m(I) + B_m(I) \tag{A8}$$

and when $J = 1$,

$$K_m(I, 1) = G_m(I) - B_m(I) + (\Delta\tau)[\alpha_m(I) - \gamma_m(I)] + (\Delta\tau)^2[\beta_m(I) - \delta_m(I)]. \tag{A9}$$

A solution of this pair of equations for $G_m(I)$ and $B_m(I)$ correct to $O(\Delta\tau^2)$ can be constructed using an iterative process. Let $G_m^{(0)}(I)$ and $B_m^{(0)}(I)$ be the solutions of Eqs. (A8) and (A9) with $\Delta\tau = 0$. The zeroth iterate, which is correct to $O(\Delta\tau^0)$, is given in this manner by

$$\begin{aligned} G_m^{(0)}(I) &= \tfrac{1}{2}[K_m(I, 0) + K_m(I + m, 1)], \\ B_m^{(0)}(I) &= \tfrac{1}{2}[K_m(I, 0) - K_m(I + m, 1)]. \end{aligned} \tag{A10}$$

With these expressions, zeroth iterates to $\alpha_m(I)$, $\beta_m(I)$, $\gamma_m(I)$, and $\delta_m(I)$ can be calculated by replacing $G_m(I)$ and $B_m(I)$ in Eqs. (A4)–(A7) with $G_m^{(0)}(I)$ and $B_m^{(0)}(I)$ respectively. The first iterate to $G_m(I)$ and $B_m(I)$, correct to $O(\Delta\tau)$, can be calculated from Eqs. (A8) and (A9) by ignoring the term that is $O(\Delta\tau^2)$ and replacing $\alpha_m(I)$ and $\gamma_m(I)$ with their zeroth iterates. The result, which is correct to $O(\Delta\tau)$, is

$$\begin{aligned} G_m^{(1)}(I) &= G_m^{(0)}(I) - \tfrac{1}{2}\Delta\tau(\alpha_m^{(0)}(I) - \gamma_m^{(0)}(I)], \\ B_m^{(1)}(I) &= B_m^{(0)} + \tfrac{1}{2}\Delta\tau[\alpha_m^{(0)}(I) - \gamma_m^{(0)}(I)]. \end{aligned} \tag{A11}$$

This process can be continued until the second iterate, correct to $O(\delta\tau^2)$,

$$\begin{aligned} G_m^{(2)}(I) &= G_m^{(0)}(I) - \tfrac{1}{2}\Delta\tau[\alpha_m^{(1)}(I) - \gamma_m^{(1)}(I)] - \tfrac{1}{2}(\Delta\tau)^2[\beta_m^{(0)}(I) - \delta_m^{(0)}(I)], \\ B_m^{(2)}(I) &= B_m^{(0)}(I) + \tfrac{1}{2}\Delta\tau[\alpha_m^{(1)}(I) - \gamma_m^{(1)}(I)] + \tfrac{1}{2}(\Delta\tau)^2[\beta_m^{(0)}(I) - \delta_m^{(0)}(I)] \end{aligned} \tag{A12}$$

is obtained. At this point, the $G_m(I, J)$ and $B_m(I, J)$ can be calculated individually to $O(\Delta\tau^2)$. The process of filtering the numerical instability out of the solutions is just that of replacing the $F_m(I, J)$ by the $G_m(I, J)$ in the two J-steps available.

ACKNOWLEDGMENTS

It is a pleasure to acknowledge K. Ogilvie and J. D. Scudder for providing their ISEE-1 electron spectrometer data before publication. All members of the Information Analysis and Display Office at

GSFC have been helpful. Special thanks to R. Thompson for providing routines which were used for interpolation and smoothing and to L. Salter for providing the 3-D plotting routine. My deepest appreciation to A. K. Tolbert.

REFERENCES

1. *IEEE Trans. Geosc. Electron.* **GE-16** (3) (July, 1978).
2. See special section, "Upstream Waves and Particles," *J. Geophys. Res.* **86** (1981), 4319.
3. K. W. OGILVIE, J. D. SCUDDER, AND M. SUGIURA, *J. Geophys. Res.* **76** (1971), 8165. W. C. FELDMAN, J. R. ASBRIDGE, S. J. BAME, AND M. D. MONTGOMERY, *J. Geophys. Res.* **78** (1973), 3697. G. K. PARKS, E. GREENSTADT, C. S. WU, C. S. LIN, A. ST.-MARC, R. P. LIN, K. A. ANDERSON, C. GURGIOLO, B. MANK, H. REME, R. ANDERSON, AND T. EASTMAN, *J. Geophys. Res.* **86** (1981), 4343.
4. A. J. KLIMAS AND J. COOPER, *Phys. Fluids* **26** (1983), 478.
5. G. KNORR, *Z. Naturfosch.* **18a** (1963), 1304.
6. A. J. KLIMAS, *J. Math. Phys.* **20** (1979), 2131.
7. R. COURANT AND D. HILBERT, "Methods of Mathematical physics," Vol. 2, p. 424, Interscience, New York, 1962.
8. T. P. ARMSTRONG, R. C. HARDING, G. KNORR, AND D. MONTGOMERY, "Methods in Computational physics," Vol. 9, p. 29, Academic Press, New York, 1970.
9. J. DENAVIT, *in* "Proceedings of the Fourth Conference on Numerical Simulation of Plasma" (J. P. Boris and R. H. Shanny, Eds.), p. 305, 1970.
10. J. DENAVIT AND W. L. KRUER, *Phys. Fluids* **14** (1971), 1782.
11. G. JOYCE, G. KNORR, AND T. BURNS, *Phys Fluids* **14** (1971), 797.
12. G. JOYCE, G. KNORR, AND H. K. MEIER J. *Comput. Phys.* **8** (1971), 53.
13. C. Z. CHENG AND G. KNORR, *J. Comput. Phys.* **22** (1976), 330.
14. R. R. J. GAGNÉ AND M. M. SHOUCRI, *J. Comput. Phys.* **24** (1977), 445.
15. M. M. SHOUCRI, *Phys Fluids* **22** (1979), 2038.
16. J. COOPER AND A. J. KLIMAS, *J. Math. Anal. Appl.* **75** (1980), 306.

Univ. Press, London, 1958.
22. See Armstrong *et al.*, [5, p. 33], and [7].
23. J. COOPER, Dept. of Mathematics, University of Maryland, College Park, Maryland, private communication.
24. E. ISAACSON AND H. KELLER, "Analysis of Numerical Mathods," p. 316, Wiley, New York, 1966.
25. Private communications: D. A. GURNETT, Dept. of Physics and Astronomy, University of Iowa, Principal Investigator, "The ISEE-1 and ISEE-2 Plasma Wave Experiments," C. C. HARBEY, Observatoire de Paris, Meudon, France, Principal Investigator, "The ISEE Electron Density Experiment."
26. R. C. DAVIDSON, "Methods In Nonlinear Plasma Theory," p. 101, Academic Press, New York/London, 1972.